

NOVEL METHOD FOR UNPOLYMERIZED PREPREG RECYCLING USING SUPERCRITICAL CO₂ EXTRACTION

Sophie Martin^a, Henry-Pierre Guriec^a, Sandy Moisan^a

a: Nantes Université, IRT Jules Verne, 44000 Nantes, France – sandy.moisan@irt-jules-verne.fr

Abstract: *For the first time, supercritical CO₂ extraction, already an industrial process, was used to remove some components from uncured prepreg. This innovative approach allows to produce a new type of secondary raw material useful for thermoplastic (TP) or thermoset (TS) composite applications without any damage on the fibres and remove the stacking behaviour of the prepreg. IMA/M21E (UD) from Hexcel uncured prepreg, available in large quantity in aeronautic industry was chosen as model. Firstly, uncured prepreg is cut at desired length. Then supercritical CO₂ extraction is performed under 40°C and 29 MPa in a semi-continuous equipment for ten hours to remove partially bisphenol A, F and aminophenol. Recycled carbon fibres (rCF) still embedded inside prepreg components (32wt% of matrix) ready to be used are so recovered. Depending on the cutting size at the beginning, several application examples are presented.*

Keywords: recycling; uncured prepreps; supercritical CO₂ extraction

1. Introduction

Prepreg-based production wastes from cut-off or out-of-date are an issue in aerospace industry. Today, they are currently landfilled or incinerated [1]. Several options for their reuse were developed at demonstrator level for sporting and recreation equipment, non-critical aerospace and automotive structures are obtained [2]. For such options, uncured thermosetting prepreg wastes must be kept at low temperature, until they are cut in chips form and moulded. The second option consists on recycling the material to recover the carbon fibre (CF) as it is done for cured materials. Several well-known ways can lead to this objective: the mechanical recycling, the thermal recycling, which include pyrolysis, and the chemical recycling [3] [4]. For instance, hydrolysis of epoxy matrix to recover the CF can be done with water as solvent at sub- or supercritical state, i.e. near or above the critical point of water, at high temperature and pressure (380°C and 220 bar), to avoid the use of organic solvents. Supercritical fluids are interesting media for chemical reaction as they have properties intermediate between liquid and gas: low viscosities, high transport properties, high diffusivities; their solvent power is dependant also of the pressure [5]. Water in particular can support ionic, polar non-ionic or free-radical reactions, so that it is said to be an adjustable solvent [6], and it is inexpensive, recyclable, and non-toxic, compatible with the principles of “green chemistry” [7]. Hydrolysis of composites based on CF and epoxy resin with sub-critical water has been performed by Aymonier et al. [8] allowing to obtain fibres with good mechanical properties. But this process is conducted under highly corrosive conditions, is energy-intensive and still at lab-scale or pilot-scale [9].

The first breakthrough of our approach is to use industrial scale process for making the recycling. Supercritical CO₂ (sc-CO₂) extraction is one famous process used at industrial scale for extraction of caffeine from coffee, neutralization of cork for wine storage, textile dyeing, degreasing... Indeed, the sc-CO₂ point is very low (31°C, 74 bar), compared to supercritical water. Due to its chemical structure, sc-CO₂ is a bad solvent, but very selective [10], and can be simply removed by evaporation. For our concern, we explore this solvent to extract the bisphenol components from the epoxy matrix well-known to be soluble under sc-CO₂ conditions. Extraction of epoxy

resin with sc-CO₂ was already studied for cleaning purpose of metallic parts: Y. Medina-Gonzalez worked on solubilization and removal epoxy components from metallic part [11]. The optimal operating conditions were 45°C and 145 bars. Another study relates the interactions between CO₂ and epoxides by combining FTIR with quantum chemistry calculations; it shows that the Lewis acid-base interactions occurs between epoxides and CO₂ and are mainly governed by the partial charge on the oxygen atom of the epoxides. The solubility of model epoxy molecules were determined in the range of 40 to 100°C until 200 bar using specific FTIR equipment [12]. Another study related the solvation effect of CO₂ and its effect on the curing temperature of model epoxy resin [13]. It seems that CO₂ get a plasticization of epoxy resin but doesn't change the reactional mechanism. In addition, pressure seems not having any significant effect. Finally, an article relates that pressure of CO₂ accelerates the polymerization reaction [14]. The conclusion is that sc-CO₂ can diffuse easily inside uncured prepreg and could help the polymerization reaction. Regarding these studies, a counterbalance must be found between favouring the solubilization versus polymerization limitation. The temperature must be as low as possible to avoid the polymerization reaction and a potential reaction with CO₂. But it should be high enough to get high density to favour solubilization. It depends on the formulation of the epoxy resin, and in all studies, the considered material is model pure epoxy. In an industrial material, uncured epoxy is composed of more than 2 components, and in this study, it is known that aminophenol and bisphenol A are part of the composition of the epoxy matrix, and they are soluble (at 40% and 50%) in sc-CO₂ [15] [16]. The use of sc-CO₂ could lead to a partial extraction of the polymer matrix, and the remove of some constituents of the formulation would block the polymerization reaction.

The second breakthrough is to not clean as much as possible the CF to allow a more easily processability. It could also help to improve the interaction with the matrix for the reuse. But tacky aspect of uncured prepreg must be removed also to get a more easily processability.

This study presents how an already industrial process, sc-CO₂ extraction, can be used to remove bisphenol A and aminophenol from a real epoxy resin from uncured prepregs. The rCF thus recovered can be reincorporated in thermoplastic (TP) and thermoset (TS) processes like thermocompression and contact moulding.

2. Materials and methods

2.1. Materials

The material for this study is IMA/M21E prepreg used by Airbus for its A350 program. It is made of unidirectional continuous high tensile strength CF IMA-12K, pre-impregnated with Hexply® M21E thermosetting epoxy. It has a resin content of 34% by weight and a fibre weight of 268 g/m². Prepreg is stored with its paper protection under -18°C. Two width are cut with a Zund equipment: 6 mm and 10 cm. 6 mm is chosen as a standard size for compound incorporation (done in Repair3D by Centexbel but not showed here).

Regarding the formulation of M21E resin, no public information is found contrary to M21 [17] [18]. M21 formulation is described as follow: three types of epoxy (bisphenol F, aminophenol, amine), one hardener (amino sulfone) and blended with two thermoplastic polymers (PES and PA6/12) (*Table 1*). We assume that M21E formulation is close to M21's one with more than 30% in wt TP content (E= enriched) to improve impact strength or toughness of composites. That

gives some indication regarding prepreg's nature, which is important to understand the next extraction process. Nevertheless, no quantitative study is completed.

Table 1: Components of the M21 epoxy formulation [17] [18]

Types/Names			Weight % content
Resin	Diglycidyl ether bisphenol F	DGEBF	15-20 wt%
	Triglycidyl meta aminophenol	TGMAP	20-30 wt%
	Para-glycidyl amine	PGAm	5-15 wt%
Hardener	4-4'-diaminodiphenyl sulfone	DDS	15-20 wt%
Thermoplastic blend	Polyethersulfone	PES	10-20 wt%
	Polyamide 6/12	PA 6 /12	3-10 wt% ratio 80%/20%

2.2. Supercritical CO₂ extraction

The operating conditions are defined regarding the balance between solubility and polymerization, to run the process at 40°C with an extraction pressure of 290 bars [15]. The extraction occurs in a semi-continuous pilot scale reactor (Figure 1). CO₂, stored in a liquid state, is compressed and pre-heated to get the desired properties. Then, it passes through a reactor full of prepreg (4L) with 10kg/h flow rate. Molecules extracted from prepreg are collected via the separator. CO₂ is then condensate and restart again the loop. CO₂ is recycled at 95% (5% are lost during the extraction). The reaction is stopped when 100kg/kg of CO₂ ratio is obtained (general rule for extraction). After the extraction, rCF are recovered free of solvent and “dry” (not tacky anymore).

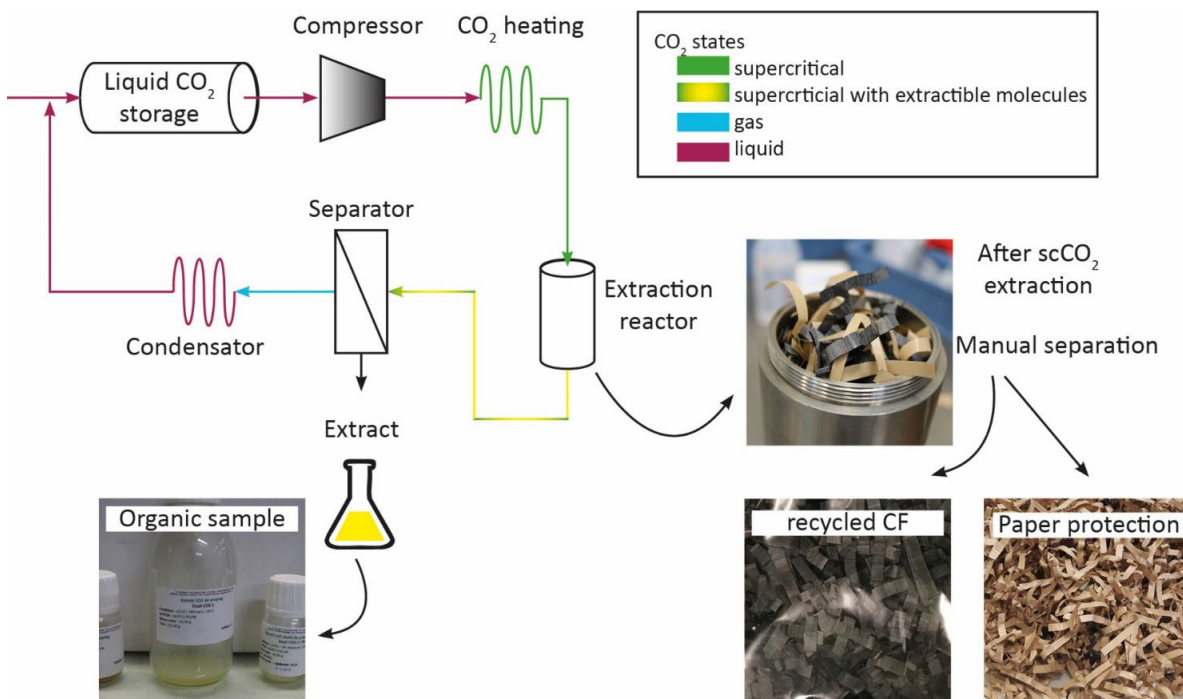


Figure 1: Schema of the extraction using sc-CO₂





2.3. Reuse of rCF with TS or TP processes

Thermocompression was tested with the consolidation of 6 mm rCF with polyamide PA6 film at 280°C during 15 minutes under 10kN of pressure with a 50T Pinette PEI press, to observe interface between CF and matrix. PA6 was chosen because it is a part of prepreg (Table 1).

To assess the rCF reuse with epoxy matrix (Araldite® LY 50-52), plates are done by contact moulding with pump down. The resin is first mixed with the hardener (Araldur®) with a proportion of 100g of resin for 38g of hardener, and then left to rest 10 minutes under vacuum to remove gas and avoiding bubbles formation. Fibres are placed in a vessel and mixed manually with the good amount of resin. A 250x250 mm marble, which contain the mixture, is placed under vacuum in an oven at 60°C during 6h. After curing, plate is demoulded and post-cured at 100°C during 4h.

To check the interest of our rCF, comparison with (i) pristine CF (pCF) 6 mm FT300-3k, (ii) fresh uncured prepreg (U-PREG), (iii) cured prepreg (C-PREG) is done (Table 2).

Table 2: pristine carbon fibres (pCF), b) sc-CO₂ rCF (rCF), c) uncured prepreg (U-Preg) and d) cured prepreg (C-Preg)

pCF	rCF	U-Preg	C-Preg
FT300-3k	IMA+org. Materials	IMA-M21E	IMA-M21E
Dry fibre	After scCO ₂ extraction	Fresh	Cured (vacuum/180°C/2h)
			

For each type of fibre, the amount of resin was calculated to obtain a fibre volume fraction of 25%, considering the presence of epoxy inside the prepregs fibres (rCF, U-Preg and C-Preg), estimated to 34% wt of resin in the whole materials. The quantity of matrix for the plate with pCF is so more important than for the other types of fibres, to obtain the same fibre volume fraction for each plate and being able to compare them. The four 250x250mm plate are done simultaneously.

2.4. Characterization

Observations on prepregs and micro cuts are made with an optical stereographic microscope Olympus, with magnification from 6.3 to 57. Analysis of CF and extracted organic molecules are performed by FTIR spectrometer Perking Elmer Spectrum One, in reflexion directly on samples. The resolution is cm⁻¹ and the results are compared with database Sadtler Spectral® and BIO RAD®. Gas Chromatography/Mass spectrometer (GC/MS) is used to analyse the organic extract. GC is a Perkin Elmer Clarus 600 apparatus, coupled with a MS Perkin Elmer Clarus 600C; products are identified with NIST 2008® database. Samples are prepared by dissolving 0.2g of organic extract in 10 ml of dichloromethane. 1µL is used for GC/MS liquid injection. The morphology is determined by SEM using a Philips Quanta Inspect microscope with W filament 25 kV equipped with Edax Genesis.

3. Results and analysis

The extractions are conducted seven times varying the volume reactor (2/4L) and the width. The process is well reproducible (Trials 4 to 7 -Table 2) for the 4L and 6 mm rCF, with a yield of 8% in weight (considering the matrix weight and not the prepreg weight). It is quite low but enough for stopping the polymerization reaction, as the samples after extraction have totally lost their tackiness behaviour at ambient temperature. This is one of the biggest advantages of our innovative process to easily store and process such type of rCF.

Better yields are obtained for 6mm samples compared to 10 cm (Table 3) even if the loading for 10 cm is more important.

Table 3: Trials performed for sc-CO₂ extraction at 40°C and 290 bar

Trials	Reactor	Load g	Granulometry	Yield%
1	2 L	140	10 cm	2.4
2	2 L	300	6 mm	5.9
3	2 L	583	10 cm	4.3
4	4 L	870	6 mm	8.4
5	4 L	889	6 mm	8.0
6	4 L	887	6 mm	8.0
7	4 L	885	6 mm	8.0

Table 4: Peaks from FTIR comparison between organic mix after extraction and bisphenol F diglycidyl ether (Ruetapox)

Molecule	Characteristic peaks also present on FTIR spectra of organic mix (cm ⁻¹)								
Ruetapox 0158	3002	2922	1610	1582	1509	1451	1345	1297	1241

Table 5: peaks from GC/MS diagram of organic mix recovered after scCO₂ extraction from prepreg

Retention time (min)	29.56	30.6	31.66	32.66
Molecule	Aminophenol	Bisphenol F	Bisphenol F	Bisphenol A

Regarding the organic molecules analysis, only a qualitative analysis can be done with FTIR and GC/MS. Bisphenol F diglycidyl ether DGEBF (Ruetapox) were detected by FTIR analysis. GC/MS diagram shows that the organic mix is mainly composed of bisphenol F, bisphenol A and Aminophenol (TGMAP) (Tables 4 and 5). It means that, regarding the Table 1, sc-CO₂ is able to extract two components from M21E (DGEBF and TGMAP). The limited number of molecules is a great advantage for a potential valorisation contrary to classical solvolysis where minimum of 10 components (phenol aniline, quinolone, ketone derivatives) are detected [8]. Nevertheless, the extraction efficiency is only 8% in weight considering the matrix weight; sc-CO₂ is not able to extract 100% of its soluble molecules due to its bad solvent properties as already mentioned.

Regarding the rCF analysis, by comparing the images before and after scCO₂ extraction (Figure 3), CF are still embedded inside a matrix as expected. Some particles are observed on the rCF surface after extraction.

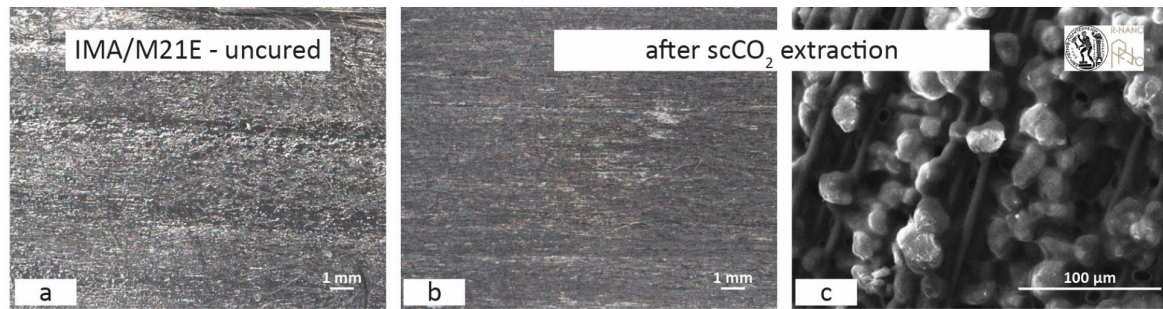


Figure 2: Optical Images of uncured prepreg before and after scCO₂ extraction (a and b); SEM image of rCF after scCO₂ extraction (c)

FTIR analysis shows that these nodules are PA6 and PES thermoplastics. This could be a limitation for the reincorporation: the matrix must be compatible with the remanent molecules. But it is also an advantage in terms of processability: the rCF are not volatile, which is one issue when rCF are totally clean. Further investigation needs to be done to analyse the remanent epoxy, not detected by FTIR spectroscopy.

Another advantage is that rCF are ready to be used due the nature of CO₂. And the conditions are so low in terms of temperature that we assume that rCF conserved their mechanical properties.

Regarding the reincorporation in PA6 film by thermocompression, fibres distribution within the matrix is not homogeneous as showed by optical microscopy image (Figure 4a). However, interaction between CF and PA6 seems to be good regarding the SEM images (Figure 4 b and c).

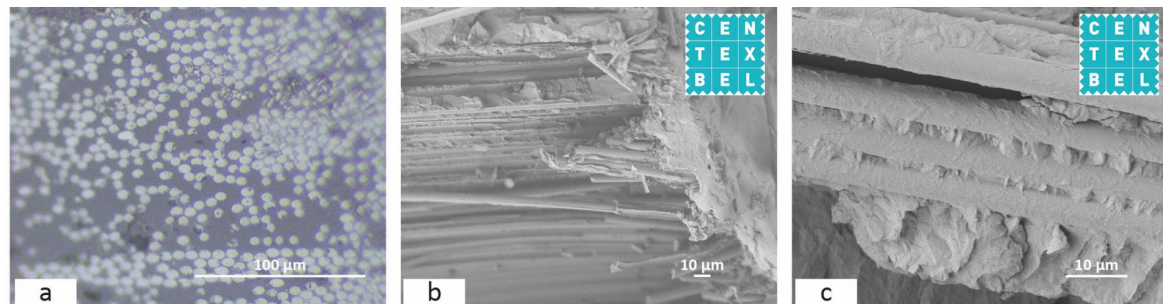


Figure 3: a) SEM and b) optical microscopy images of rCF impregnated with PA6 film

Some further investigation needs to be done to determine the link between TP and remanent epoxy components still present after sc-CO₂ extraction.

Regarding the reincorporation in TS via contact moulding, pCF shows the best repartition in the epoxy. This is due to its flexible behaviour. It is also the case for rCF (Figure 5). Nevertheless, a lot of porosity is observed, meaning that the process must be optimized before discussing the wettability behaviour between fibre and epoxy. But the proof of concept is done for reincorporation into epoxy resin. And the untacky behaviour is a huge advantage in terms of processability as already mentioned. For C-Preg, the main issue was for cutting the cured prepreg.

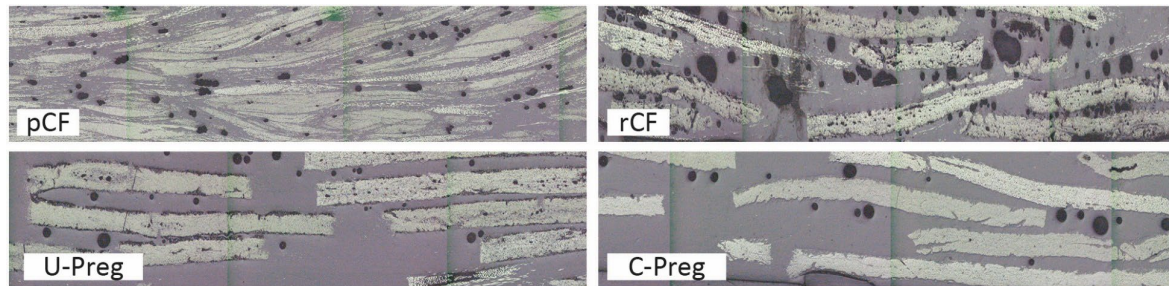


Figure 4: Micrometric cuts of a) pCF, b) rCF, c) U-PREG and d) C-PREG plates

4. Conclusions & perspectives

The use of supercritical CO₂, well-known as environmentally benign was chosen for partial extraction of the epoxy matrix of uncured epoxy prepregs, which constitute an important part of aeronautical industry wastes. Aminophenol and bisphenol A and F were partially extracted, leading to the freezing of the epoxy's polymerization. The resulting rCF was successfully included in a TP (with PA6) and TS (epoxy) processes. Further development needs to be done to measure the mechanical behaviour of the new composite.

The sustainability assessment of this process is presented in another article of this conference; it proves the benefit of this approach environmentally and costly speaking [19].

In another study, rCF are also functionalized after sc-CO₂ extraction with magnetic nanoparticles in supercritical media to bring induction heating properties, useful for repairing thermoplastic/carbon fibre composite [20].

Acknowledgements

The Repair3D project has received funding from the European Union's Horizon 2020 research and innovation programme under grant agreement N° 814588. We acknowledge the National Technical University of Athens (NTUA) and Centexbel (Belgium) for the SEM characterizations.

5. References

1. Nilakantan G, Nutt S. Reuse and upcycling of aerospace. *Reinforced Plastics* 2015; 59(1): 44-51.
2. Nilakantan G, Nutt S. Reuse and upcycling of thermoset prepreg scrap: Case study with out-of-autoclave carbon fibre/epoxy prepreg. *Journal of Composite Materials* 2018; 53(3): 341–360.
3. Sukanto H, Raharjo WW, Ariawan D and Triyono J. Carbon fibres recovery from CFRP recycling process and their usage: A review. *IOP Conf. Series: Materials Science and Engineering* 2021.
4. Oliveux G, Dandy LO, Leeke GA. Current status of recycling of fibre reinforced polymers: Review of technologies, reuse and resulting properties. *Progress in Materials Science* 2015; 72: 61-99.
5. Wu BC, Klein MT, Sandler SI. Solvent effects on reactions in supercritical fluids. *Ind Eng Chem Res.* 1991; 30: 822-828.

6. Oliveux G, Bailleul JL, Le Gal La Salle E, Lefèvre N, Recycling of glass fibre reinforced composites using subcritical hydrolysis: reaction mechanisms and kinetics, influence of the chemical structure of the resin. *Polym Degrad Stab.* 2013; 98: 785-800.
7. Anastas P, Eghbali N. Green chemistry: principles and practice. *Chemical Society reviews* 2009; 39(1): 301-312.
8. Henry L, Schneller A, Doerfler J, Mueller WM, Aymonier C, Horn S, Semi-continuous flow recycling method for carbon fibre reinforced thermoset polymers by near- and supercritical solvolysis *Polym. Degrad. Stab.* 2016; 133; 264–274.
9. PARCCA project. <https://irt-jules-verne.fr/en/projets/advanced-carbon-fibre-composite-recycling-processes/>
10. Eastoe J, Peach J. Supercritical carbon dioxide: a solvent like no other. *Beilstein J Org Chem.* 2014; 10: 1878–1895.
11. Medina-Gonzalez Y. Étude des phénomènes de solubilisation de pre-polymères de résine epoxy dans les esters d'acide gras comme biosolvants 2006.
12. Foltran S, Cloutet E, Cramail H, Tassaing T. In situ FTIR investigation of the solubility and swelling of model epoxides in supercritical CO₂. *The Journal of Supercritical Fluids* 2012; 63: 52-58.
13. Hu DD, Lyu JX, Liu T, Lang MD, Zhao L. Solvation effect of CO₂ on accelerating the curing reaction process of epoxy resin. *Chemical Engineering and Processing* 2018; 127: 159-167.
14. Lyu J, Hu D, Liu T, Zhao L. Non-isothermal kinetics of epoxy resin curing reaction under compressed CO₂. *J Therm Anal Calorim.* 2018; 131: 1499–1507.
15. Mouloungui Z, Medina-Gonzalez Y, Thiebaud-Roux S, De-Caro P, Hernandez-Ochoa L. The role of co-additive on epoxy resin pre-polymers solubilization in supercritical CO₂. *The Journal of Supercritical Fluids* 2006; 38(1): 13-17.
16. Martín Á, Rodríguez-Rojo S, de Pablo L, José Cocero M. Solubility of Bisphenol A in Supercritical Carbon Dioxide. *J. Chem. Eng. Data.* 2011; 56(10): 3910–3913.
17. Tranchard P, Duquesne S, Samyn F, Estèbe B, Bourbigot S. Kinetic analysis of the thermal decomposition of a carbon fibre-reinforced epoxy resin laminate. *Journal of Analytical and Applied Pyrolysis* 2017; 126: 14-21.
18. Paris C, Etude et modélisation de la polymérisation dynamique de composites à matrice thermodurcissables, PhD study, 2011.
19. Gkika A, Petrakli F, Vlysidis A, Karagiannis P, Moisan S, Koumoulos E, Life Cycle Assessment and Life Cycle Costing on recycled post-industrial composite waste, ECCM 2022.
20. Moisan S, Guriec HP, Martin S, Gkika A, Koumoulos E, Kainourgios P, Charitidis C, Innovative process for uncured carbon fibers prepreg recycling and functionalization with magnetic nanoparticles using supercritical fluid chemistry, ISGC 2022.

NEW TRENDS IN PLASTICS AND THERMOPLASTIC COMPOSITES UPCYCLING: THERMOPRIME® & THERMOSAIC® TECHNOLOGIES

F. Ruch^a, C. Callens^a

^a : Cetim Grand Est ; 21, rue de Chemnitz, Mulhouse, 68068, France -
frederic.ruch@cetimgrandest.fr

Abstract: *In a general context of scarce accessible material and energy resources, Cetim Grand Est developed two eco-processes for the recovery of composite and plastic waste to help reduce the environmental footprint of materials and support companies in their technological and ecological changes.*

Recycling thermoplastic composite materials with an “upcycling” approach is a way to contribute to the grow of the global thermoplastic composite market. As a lot of waste is generated during the production process of panels and preforms, finding solutions for recycling it with more added value is a real concern.

In the coming years, this work will make it possible to respond to the regulatory challenges that companies will have to face in order to optimize the use of energy and the resources available to them.

Keywords: *Thermoplastic composite ; Recycling ; Upcycling ; Thermosaic® ; ThermoPRIME®*

1. Introduction

Nowadays, the global production of composites and plastics currently amounts to 11 and 367 million tons a year, respectively [1,2]. These materials, which were developed on a large scale in the last century and have now become unavoidable, are struggling to find technically and economically viable recovery routes. What might once have appeared as a minor inconvenience is now becoming a threat to industrial activity. Indeed, the predicted scarcity of non-renewable material and energy resources [3] is leading to tighter regulations, gradually forcing the composites and plastics industries to reduce their environmental footprint. Even though the objective is the same for all, the historical context is significantly different.

The composites industry, which is not highly automated and mainly targets niche markets, produces high-value-added and long-lasting goods, made from a long or continuous fibre reinforcement (glass) and a thermosetting resin (unsaturated polyester) in nearly 90% of cases [4]. While production waste remains more or less stable from year to year despite an overall increase in production, end-of-life waste is increasing sharply as the first generations of products designed 20, 30 or 40 years earlier (boat hulls, wind turbine blades, cladding panels, etc.) come to the end of their life cycle. The sharp increase in waste deposits is not necessarily a problem in itself. However, given the infusible nature of the resin, landfill remains the only option in

in itself. However, given the infusible nature of the resin, landfill remains the only option in nearly 90% of cases [4]. This percentage has not decreased for many years, despite numerous R&D efforts in this area. Technical solutions exist, but none of them convincingly overcomes the barrier of economic viability (with the exception of composites containing carbon fibre, but they represent only a few percent of the market) [5].

This situation is no longer acceptable today. The composites industry needs to find an alternative to the thermosetting resins historically used. It is currently undergoing a transformation by innovating in the field of materials, on the one hand (for example Arkema's Elium[®] resins [6]), and in materials and processes, on the other hand, by moving closer to plastics processing. In both cases, the idea is to use thermoplastic resins, which have a higher recycling potential than thermosetting resins. However, these materials will only be massively adopted once their recyclability has been proven on an industrial scale.

The highly automated plastics industry, which is mainly aimed at mass markets, produces low-value-added and short-lived goods from thermoplastic resins. This short lifespan generates very high waste volumes every year [7]. A material recycling channel does exist, but for the moment it only manages to capture a small part of the waste stream (around 10% worldwide) [8]. Thus, on a global scale, since the 1950s, nearly 80% of waste is dispersed in nature or landfilled [9]. As before, this situation is no longer acceptable at present. The plastics industry must increase the recycling rate of its resins through the use of applications with a higher added value, by approaching the composites industry in particular.

2. What prospects for plastics and composites recycling?

2.1 Two technologies with the same production line...

This mutual understanding between two formerly compartmentalised industries offers new waste recovery prospects. In this respect, Cetim Grand Est developed two eco-technologies that meet the upcycling expectations for two kinds of materials [10].

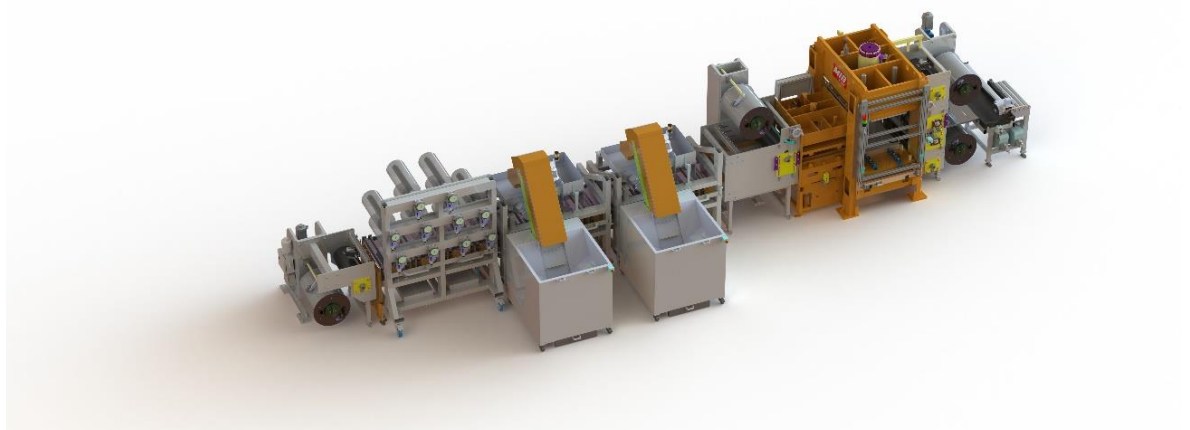


Figure 1. Thermosaic[®] and ThermoPRIME[®] process line

Using a step-by-step thermomechanical process, this innovative process (Figure 1) allows the continuous production – from waste – of recycled semi-finished products in the form of large-scale thermoplastic composite panels. The pre-industrial production line, designed in a flexible, cost-effective and versatile way, and with an “upcycling” approach, allows the recovery of various thermoplastic waste into ranges of recycled composite semi-finished products with high added value and an optimised and competitive cost/performance ratio.

Starting from the same production line, but with two different feed systems, the Thermosaïc® and ThermoPRIME® (Thermo Plastic Recycling for Innovative Material and Ecodesign) eco-technologies were developed to fully exploit the recycling potential of composite and thermoplastics materials.

2.2 Thermoplastic composite wastes: Thermosaïc® technology

Starting from a deposit of production waste (and then end-of-life products), this technology consists in shredding the material in order to maximize its economic potential for recovery. The Thermosaïc® technology (Figure 2) retains the intrinsic value of the initial composite material, continuously moulding these shreds by thermocompression into panels. Compared to recycling into short fibre compounds, Thermosaïc® panels have significantly better mechanical properties and a high formability potential.

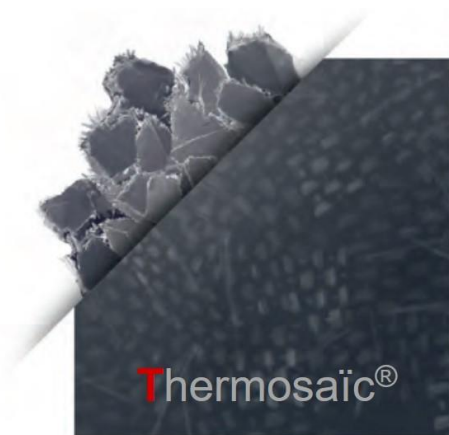


Figure 2. Thermosaïc® recycled composite

2.3 Thermoplastic wastes: ThermoPRIME® technology

Starting from a recycled plastic material with low added value, formulated to the specific needs of the application (controlled quality), ThermoPRIME® (Figure 3) consists in associating this polymer with continuous or long fibre reinforcements to produce continuous laminates with high durability and economic recovery potential.



Figure 3. ThermoPRIME® recycled thermoplastic

2.4 Industrial applications

Thermoplastic composite waste recycling has already been the subject of various studies, in particular with Porcher Industries, the aim being to find ways of recovering materials such as PPS/glass with a high added value (Figure 4).



Figure 4. Porcher PPS/GF Thermosaïc® panel

Generally speaking, the aeronautical industry shows interest in any technology capable of recycling various production waste (up to 40% waste) resulting from stamping or thermocompression operations.

With the same logic of economic optimization and reducing the environmental footprint of materials, an eco-designed laptop case demonstrator (Figure 5) made of recycled and/or bio-sourced materials is currently being developed for the fashion and luxury sector (CARATS) of the Carnot institutes.



Figure 5. Example of a laptop including thermostamped foils produced from ThermoPRIME® technology

Similarly, another development can be cited. In collaboration with the company EMI SAS [11], a recycled variant of an electric skateboard brand-named Okmos [12], has been developed, demonstrating that semi-finished products made from thermoplastic wastes can find sustainable and value-added outlets.



Figure 6. Example of an electric skateboard, based on a Thermosaic® stamped panel overmoulded with thermoplastic resin

3. Conclusion

These examples show the interest of manufacturers and academics in major subjects that meet strong societal expectations. This flexible and agile technology makes it possible to recycle all types of thermoplastics (from PP to PEEK) and reinforcements (glass, carbon, flax, etc.). It is mature enough to support industrial needs through feasibility studies, proofs of concept, specific formulations, pilot production, etc.

Acknowledgements

This article was firstly edited in 2020, with the following title: “New trends in composites and plastics recycling” (JEC Composites Magazine ; n°136 ; p.36-37). This updated version is proposed with courtesy of JEC Composites Magazine.

Cetim Grand Est would sincerely acknowledge Carnot MICA Institute, for participating to laptop and electric skateboard developments.

4. References

1. “Overview of the global composites market” ; 2017 ; JEC Group ; ISBN 978-2-9526276-7-2
2. <https://www.statista.com/statistics/282732/global-production-of-plastics-since-1950/>
3. “Indicateurs d’épuisement des ressources en analyse de cycle de vie” ; Charlotte Petiot, François Witte, Yannick Le Guern ; (Rapport de recherche) 2012-02 ; SCORE LCA. 2014. hal-02269178
4. “Recyclage des composites” ; Patricia Krawczak ; Techniques de l’ingénieur ; ref. AM5895 V1
5. <https://carbonfiberresource.com/production-capacities/>
6. https://www.arkema.com/global/en/products/product-finder/product-range/incubator/elium_resins/
7. “Production, use, and fate of all plastics ever made” ; R. Geyer, J.R. Jambeck, K.L. Law ; 2017 ; Science Advances, 3(7)
8. https://www.lemonde.fr/planete/article/2022/03/02/pollution-plastique-l-onu-fait-un-pas-de-plus-vers-un-texte-juridiquement-contrainant_6115875_3244.html
9. https://www.lemonde.fr/pollution/article/2017/07/19/depuis-1950-l-homme-a-fabrique-8-3-milliards-de-tonnes-de-plastiques_5162660_1652666.html
10. <https://youtu.be/Ga-Pm9KJ6ms>
11. <https://www.emi-wissler.com/en>
12. <https://www.okmos.fr/>

HIGH PERFORMANCE MULTI-FUNCTIONAL COMPOSITE STRUCTURES WITH INKJET PRINTED EMBEDDED CIRCUITS

Bruno, Giuntoli^a, Rajasundar, Chandran^b, Gioele, Balestra^b, Joël, Cugnoni^a

a: School of Management and Engineering Vaud, HES-SO, Switzerland (Yverdon-les-Bains, Switzerland) – joel.cugnoni@heig-vd.ch

b: iPrint Institute, HEIA-FR, HES-SO University of Applied Sciences and Arts Western Switzerland

Abstract: *Electronic is essential in functional structural components. Whether it is for power supply, data communication or structural sensing & reliability, these signals need to be connected from the source to the component's terminals. State of the art solutions use standard wiring and thermoplastic flexible PCB (printed circuit boards) presenting three main disadvantages: the increase of overall weight, structural weakening due to matrix incompatibility and the inherent dimensional and geometrical constraints. The Multi-Functional-Composite Ply (MFCP) concept tackles the state-of-the-art inconveniences of electronics systems in composite structures with an embedded structural and multi-functional composite ply integrated into a laminate. Electrically conductive circuits are inkjet printed on a thin-ply substrate prior to the integration into a CFRP structure before curing. This flexible substrate has the capability to carry power, analogic and digital signals and forms an integral part of the laminate in terms of its mechanical response.*

Keywords: Multi-Functional Structures; Smart materials; IoT; inkjet printing; conductive flexible substrates

1. Introduction

The integration of electronics in virtually any manufactured component is a reality in today's world. From an aerospace component to a household appliance, any of these elements use an electric circuit to provide power, acquire or transmit data to sensors, and communicating to onboard computers. To provide thin (>100µm), compact and reliable electronic connections, the industry state of the art in high end electronics uses flexible PCBs [1, 2]. These thermoplastic substrates (i.e. PET, PC) are the established solution to be used on exposed surfaces or internal cavities, usually adhered with relatively heavy adhesives. Thin-ply composites provide excellent mechanical properties [3, 4, 5] and open the design space allowing to integrate more individual plies into a pre-defined thickness than standard thick (>100µm) composite plies. In this work, a thin-ply inkjet-printed composite substrate is tested in unnotched tension (UNT), three-point bending (TPB) and interlaminar fracture toughness (DCB) to evaluate the mechanical and electrical limitations of the inkjet-printed Multi-Functional Composite Ply. A demonstrator of a smart wingfoil handle is also presented, integrating the mechanical and electrical capabilities of the MFCP using analogic and digital circuits embedded in the structure to acquire gyroscopic, atmospheric, and structural sensing data.

2. Materials and methods

2.1 Substrates preparation

To ensure the electrical insulation of the MFCP, a thin-ply GFRP substrate is used to adhere the inkjet printed conductive layers. This prepreg layer is cured on a standard curing cycle. The 50 μ m nominal thickness substrate is composed by a 25gsm non-oriented fiberglass mat with epoxy prepreg. The curing process is needed to provide a stable surface prior to the conductive ink-jet printing process.

2.2 Specimen design

Three series of specimens were designed for the UNT, TPB and DCB testing. All tests were supported and bonded to pre-cured GFRP 3mm plates using Gurit SA80 high toughness prepreg adhesive. The electrical design of each testing had the purpose of evaluating the relation between the mechanically exposed stressed and the electrical behavior of the MFCP conductive traces. For these tests, a glass fibre (GFRP) composite was chosen used as a model substrate to maximize the achievable strain without risks of premature failure.

2.3 Unnotched Tensile Testing (UNT) specimens

The tensile testing consisted in a 3mm support GFRP plate of 25mm by 250mm as a standard ASTM D3039 where the MFCP was bonded using Gurit SA80 under vacuum. For deformation monitoring and correlation, all samples had a strain gauge on the opposite side of the MFCP as seen on Figure 1. The inkjet-printed conductive traces were monitored for resistance variation and continuity with a four-point resistivity measuring method.

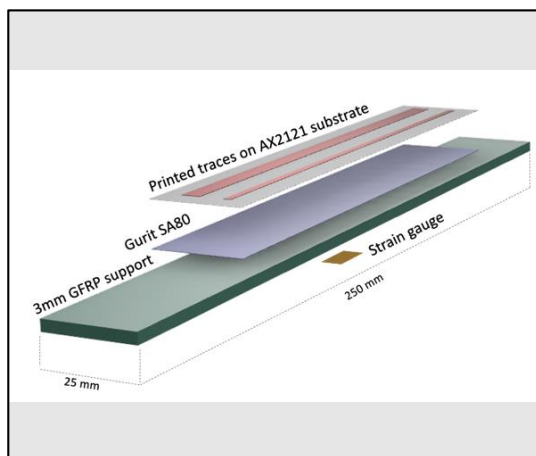


Figure 1 - Exploded CAD view of UNT specimen

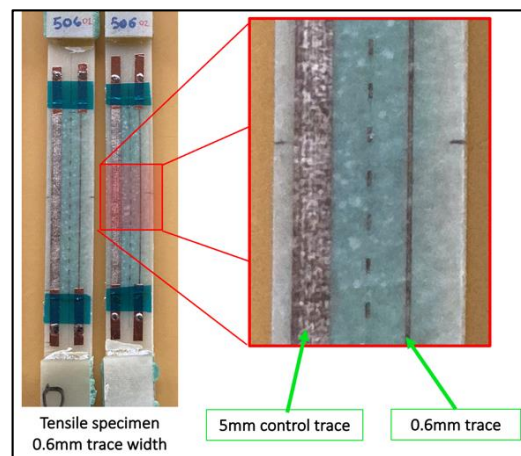


Figure 2 - UNT 506 specimen close up

Five sample patterns with width variations were designed and manufactured, with two traces on each one. The left-hand side is the reference trace and the right-hand side varies its width from 0.4mm to 5.0mm. The “UNT 506” specimen and a traces close-up can be seen on Figure 2. All specimens were inkjet printed with a two-pass process using a commercial silver nanoparticle-based Metalon[®] ink to increase electrical conductivity, as referenced on Table 1.

Table 1 - UNT specimens, traces and inkjet printing passes

ID number	Ref. Trace width (rL)	Variable trace width (rR)	Number of passes
504	5 mm	0.4 mm	2
506	5 mm	0.6 mm	2
510	5 mm	1.0 mm	2
520	5 mm	2.0 mm	2
550	5 mm	5.0 mm	2

2.4 Three-point bending testing (TPB)

Analog to the UNT test, the TPB testing has a pair of traces to monitor the variation of the resistance under the loading and unloading phases as shown on Figure 3. On the other hand, the placement of the strain gauge on the TPB is as close as possible to the inkjet printed traces on the tension side to capture the strain and resistance variations as linearly as possible. For this test, 5mm parallel traces pairs were printed to acquire two resistance values for the same specimen. This resistance variation ($\Delta\Omega/\Omega$) is evaluated on a pseudo static and short cycle fatigue test schedule using a Shimadzu 20kNX tabletop universal machine.

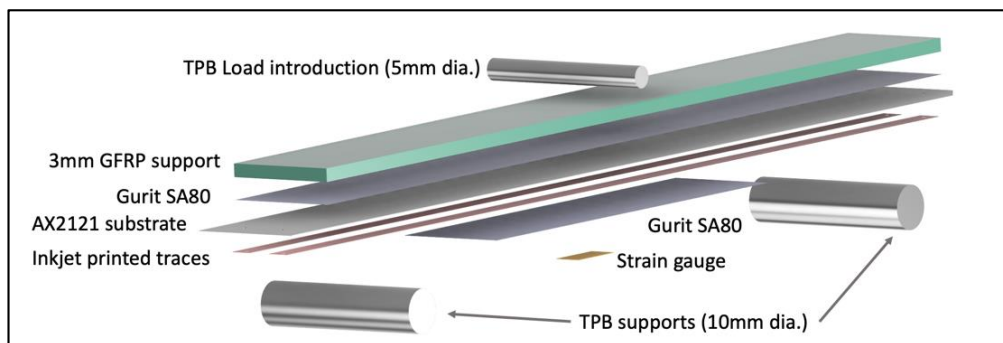


Figure 3 – Three-point bending specimen exploded view

2.5 Inter-laminar Toughness (DCB) on “Zebra” specimen

The Zebra DCB test aimed to evaluate the inter-laminar strength impact of traces width and spacing on a MFCP. Four patterns with 30mm cycle length section and one third printed area is evaluated as seen on Figure 4. A reference “raw” sample without any print or exposure was also prepared and tested on the same manner.

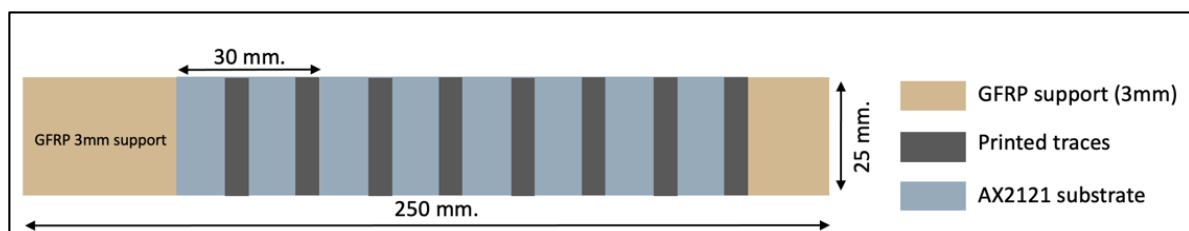


Figure 4 – Top view of general Zebra DCB specimen

The traces widths of 1.0, 2.0, 2.5 and 5.0mm were evaluated as shown on Figure 5. The MFCP specimen were integrated to a DCB testing setup, following ASTM D5528 standard with a pre-crack length of 50mm using non-perforated ETFE film. All interlayers were bonded with Gurit SA80 pre-preg adhesive and cured under full vacuum.

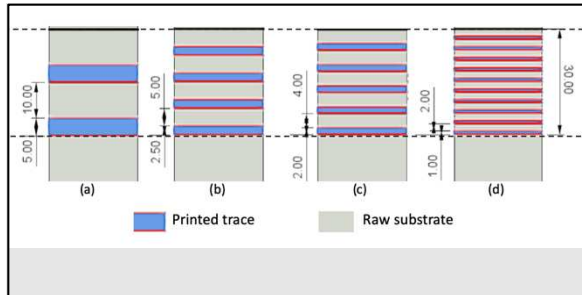


Figure 5 -Zebra specimen 30mm length patterns

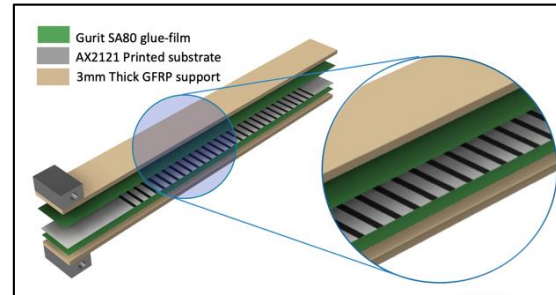


Figure 6 – DCB Zebra specimen assembly

2.6 Inkjet printing of MFCP

A twin trace pattern as seen in Figure 1, Figure 2, Figure 3 as well as the Zebra patterns seen on Figure 5 were printed over the 25 mm x 250 mm composite substrates. The conductive ink used was a water-based silver nanoparticle ink Metalon[®] from Novacentrix. A custom-built printer platform fitted with a piezo-based DOD Ricoh inkjet print head and an Adphos near infrared lamp (9.3 kW air cooled module) for the curing was used. Several printing trials were performed with different print resolutions and curing conditions. The most favorable conditions for print quality and conductivity were optimized for multi-pass 1200 dpi print resolutions leading to surface resistances on an average less than 0.2 Ohms per square.

3. Results and discussion

3.1 UNT Results

The pseudo static tensile tests were conducted until 0.8% strain on all samples. The results seen on Figure 7 show a direct resistance measurement in Ω (Ohms) vs Strain (%) for both the Left-hand side reference traces (5mm) and the variable width traces on the Right-hand side presented on Table 1.

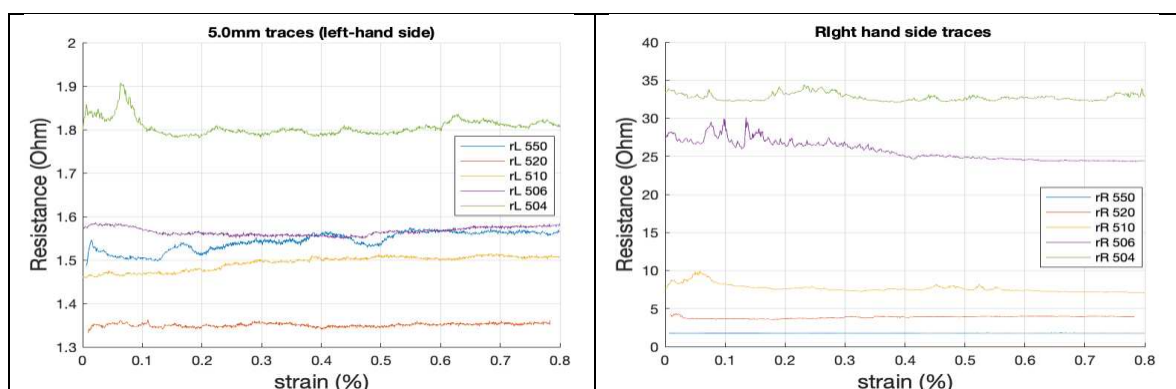


Figure 7 – Resistance (Ω) vs. strain (%) on UNT tensile tests

The left-hand side traces at 5mm width present little variation between the specimens, for inkjet-printed conductive traces ($<0.5\Omega$). On the right-hand side, the narrower traces show higher resistance values and present higher “noisy” peaks, specially at lower strain values.

The signal presents considerable variations no systematic tendency of resistance increase. Several phenomena could explain these variations. First, it is important to note that the electric conduction in such printed traces is carried out by local bonds between partially sintered nanoparticles. Thus, during the first cycle, a preconditioning effect can happen in which weak bonds can break but also particles contacts can rearrange with strain. Moreover, creating a perfect bonding between the measurement probes and the traces is difficult due to their very sensitive nature (a few nm thickness), and thus small contact resistance variations could also affect the readings. Nevertheless, the main finding is that, even though not suitable yet for sensing, the printed traces remain reliable for data transfer or low current power supply under a high strain of 0.8% which is usually beyond the onset of damage of typical CFRP composite laminates.

3.2 Three Point Bending results

The cyclic testing results gave a new perspective to the use of the MFCP. While the main objective being the evaluation of the Metalon inkjet-printed traces capabilities for design allowances at 0.5% strain, the plotting results of the 500 cycles Strain (%) vs $\Delta\Omega/\Omega$ (%) observed on Figure 8 presented a linear relation between them. While not perfectly equivalent due to the inkjet printing process variations, the 0.175 Ω/cm and 0.21 Ω/cm static measured resistances of the parallel traces could be potentially used as an embedded strain measurement component.

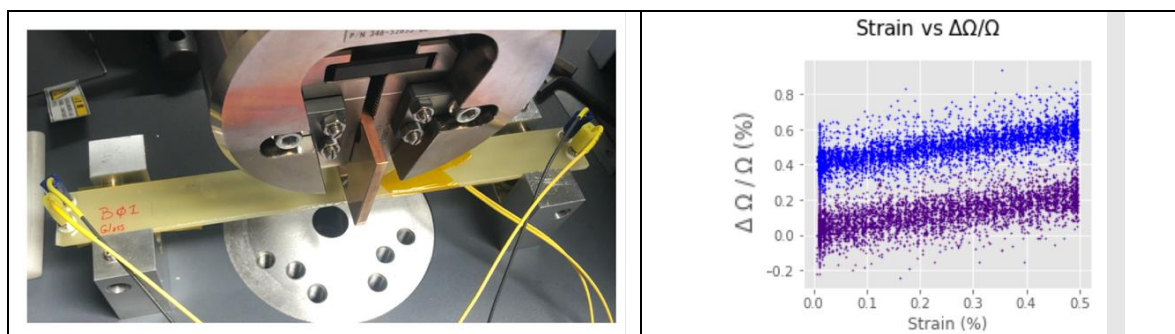


Figure 8 - TPB test and cyclic results

The plots on Figure 9 show the stability of the Multi-Functional Composite Ply on a 1000 cycles pseudo-fatigue testing schedule. The average variation of +/- 0.17% on both specimen shows the stability of the resistive performance.

The TPB test cycle shows a much more stable relative resistance variation results than the UNT results on section 3.1. Subsequent tests not shown on this work lead to evaluations at 0.8% strain, providing equivalent results, without a damage to the MFCP.

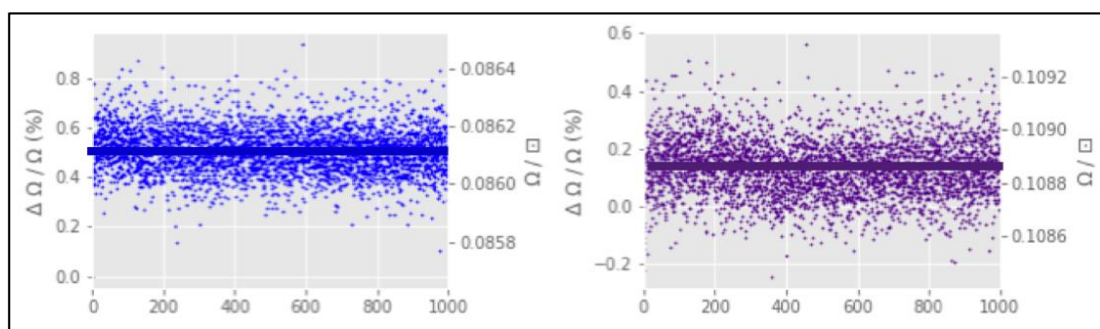


Figure 9 - Resistance variation vs cycles @ 0.5% strain

3.3 Zebra DCB testing results

The results of this non-conventional DCB test were surprisingly below expectations. The Load vs. Crack opening (displacement) plot on Figure 10 presents less but more abrupt sawtooth peaks on the 5mm traces specimen (black) than on the 1mm width traces specimens (green). This result could be explained by the higher number of sections on the smaller width traces specimen and extrapolates to the other two intermediate traces width specimen (2.0mm and 2.5mm). With a one third of the total surface made of weak printed traces, a 33% critical ERR reduction is expected when compared to the blue non-printed raw specimen. The critical ERR results observed on Figure 11 show a reduction of $\approx 55\%$ in all patterns, with a small advantage on the 1.0mm traces.

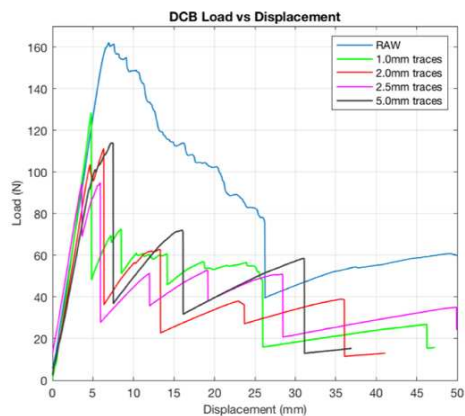


Figure 10 - DCB Load-Displacement on Zebra specimen

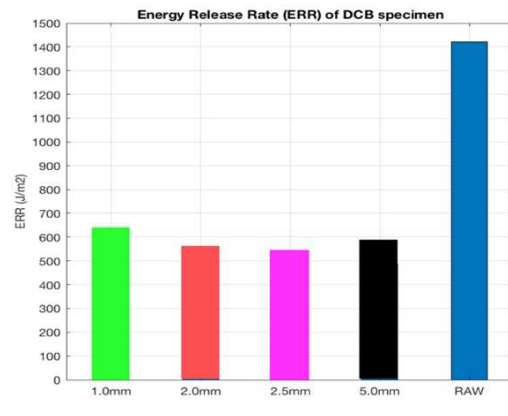


Figure 11 - ERR on Zebra specimen samples

A hypothesis on the large ERR drop phenomena is the fact that the inkjet-printed substrates are cured with a NIR (Near Infra-Red) light. This exposure of a fraction of a second to the IR light could be the cause of the matrix deterioration and its mechanical properties. Nevertheless, even with an extreme 33% of printed surface, the level of mode I interlaminar toughness of the MFCP remains sufficiently high compared to values observed in CFRP laminates and thus can be used in many applications without creating a weak point in terms of delamination.

4. Integration and demonstrator

4.1 Objectives

The objective to this demonstrator was the integration of the multiple capabilities of the MFCP. Using a sport support, such as the wingfoil is the perfect benchmark test as it combines the complexity of a reduced geometrical design space, and the challenge of a lightweight solution. The chosen wingfoil wing for the prototype is a Duotone Slick being the only wing in the market with a CFRP tubular handle. The goal of the prototype was the integration of the Multi-Functional Composite Plies into the thin-ply CFRP prepreg 26mm diameter tubular structure.

4.2 Electronics block diagram & interconnectivity

The MFCP electrical interconnection seen on Figure 12 consists in three main elements; The data acquisition unit embedded into the handle, managed by an ESP32 microcontroller with wireless and I2C capabilities; a Raspberry Pi Zero used as a server for wireless data acquisition and clients connectivity and one or multiple clients (i.e. cellphone) to read the live data or access the log.

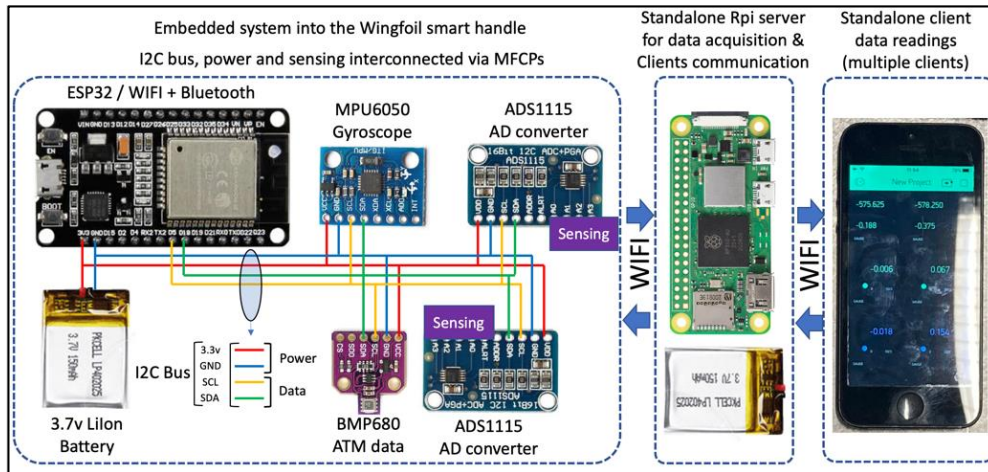


Figure 12 - Block diagram of demonstrator

The manufacturing of the thin-ply prepreg CFRP tube with MFPCs was done with a ply-by-ply method with intermediate debulks using a CNC machined female mold and cured at 7Bar. The I2C bus, composed by 4 conductors is placed in the internal face of the tube and interconnects all sensors reliably as seen on Figure 13.

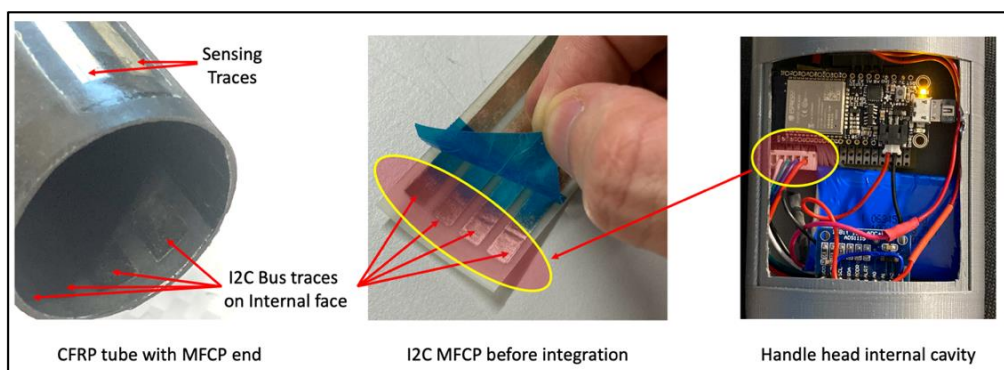


Figure 13 - I2C bus and Sensing traces

The final integration with the wingfoil wing and smart handle with MFPC handle can be seen on Figure 14 where the sensing traces are exposed to the tension side of the tube loading. While the systems are up and reliable, both electrically and mechanically, in land testing is ongoing on the prototype.



Figure 14 - Final installation of the Smart Handle into the Duotone Slign Wing

This prototype has proven the feasibility and reliability of the MFCP integration into a compact thin-ply and fully functional CFRP principal structure. Both mechanically and electrically, this prove of concept shows the potentials of the technology.

5. Conclusions

This work presents a solution to functionalize composite structures by embedding a thin-ply multifunctional ply (MFCP) into composite structure typically made of CFRP epoxy composite prepregs. A key challenge is to ensure that the embedded MFCP does not introduce a weakness in the composite laminate and can provide reliable electric functions up to the onset of damage of the laminate. The results from the tests shown in this work demonstrate that the developed MFCP provide stable electric functions for data transmission and low power electronics up to 0.8% strain in both static and low cycle fatigue while maintaining a mode I interlaminar toughness higher or equal to most CFRP laminates. Being very thin, the MFCP ply can be easily conformed and integrated in the prepreg stacking sequence of parts with relatively high curvature. Specific solutions have also been developed to integrate and connect the MFCP printed traces (through the thickness via, interface with surface mount components) which opens a large spectrum of potential applications, from consumer products and sports to the aerospace and defense industry. Since the series of tests presented in this work, different inkjet printing techniques, parameters and settings have been adapted to optimize the electrical stability and mechanical performance of the printed traces.

Acknowledgements

HEIG-VD and HEFR thank the EcoSwissMade program of HES-SO for supporting this work.

References

1. Wetzel ED. "Reducing weight: multifunctional composites integrates power, communications and structure". AMPTIAC Quarterly 2004;8(4):91-5
2. A. Duarte et al., "Multifunctional Materials Systems: A state-of-the-art review". Composite Structures, Vol. 151, paper number, pp 3-35, September 2016.
3. R. Amacher, J. Cugnoni, J. Botsis, L. Sorensen, W. Smith, C. Dransfeld. Thin ply composites: experimental characterization and modeling of size-effects. Composites Science and Technology, 101,121-132, 2014
4. R. Teixeira, S. Pinho, P. Robinson. Thickness-dependence of the translaminar fracture toughness: Experimental study using thin-ply composites. Composites Part A. 90, 2016.
5. R. Amacher et al., Toward aerospace grade thin-ply composites, Proceedings of 17th European Conference on Composite Materials (ECCM17), Munich, Germany, June 2016
6. M. Jalalvand, G. Czél, M. R. Wisnom. Damage analysis of pseudo-ductile thin-ply UD hybrid composites - A new analytical method. Composites: Part A, 69, 83-93, 2015

VALIDATING SIMULATED RESIDUAL STRAINS DUE TO THERMOFORMING USING FBGS

Michael, Paulitsch^a, Maximilian Pollak^a, Christoph Zanghellini^a, Johannes Jungbauer^a, Franz Maier^a, Roland Hinterhölzl^a

a: Research Group of Lightweight Design and Composite Materials, University of Applied Sciences Upper Austria, Stelzhamerstraße 23, 4600 Wels, Austria – Michael.Paulitsch@fh-wels.at

Abstract: *Accurately determining process induced residual strains in carbon fiber reinforced plastic (CFRP) and CFRP-metal hybrids is vital for understanding the behavior of manufactured components and to validate simulations of process induced deformations. The required local strain measurements for this task can be obtained with Fiber Bragg Gratings (FBGs), embedded between CFRP layers. The required strain and temperature calibrations is carried out in a tensile testing machine. FBGs were used to monitor the manufacturing process of CFRP and hybrid plates in a thermoforming station until demolding. Good agreement in terms of strain results and visibility of major effects such as crystallization behavior between measurement data and process simulation results has been achieved.*

Keywords: FRP-metal hybrid; FBG; Process simulation; Thermoforming; Residual stresses

1. Introduction

FBGs are fiber optical sensors using a Bragg grating, i.e., a periodical modulation of the refractive index in the core of the fiber. Changes in the state (temperature, strain, pressure) of the embedding material result in a deformation of the grating and cause a modulation of the wavelength of the reflected light. FBGs have been used for process monitoring and structural health monitoring in various CFRP components [1–3] and have also been applied in Fiber Metal Laminates (FMLs) [4]. They are placed between layers and measure the local strain the direction of the FBG, to validate cool- down- and warpage- simulations by comparing the measured strain to the predicted strain in the simulation.

2. Materials

For this study, carbon fiber reinforced plastic (CFRP) and CFRP-metal hybrid plates with a length of 200mm, width of 100mm and a total thickness of 4 mm were manufactured. The constituents were UD carbon fiber reinforced PA6 (SIGRAPREG®TP C U157-0/NF-T340/46%) and 2 mm 1.4301 stainless steel or EN AW-1050A aluminum (Al) sheets. For hybrid components, an approximately 25µm thick layer of the adhesion promoter Vestamelt Hylink (Evonik) was deposited onto the sandblasted metal surfaces. The investigated layups are summarized in *Table 1*.

Table 1 Layups of investigated CFRP and hybrid plates

O ₂ /90 ₂ /O	TC, FBG	0/90 ₂ /0 ₄ /90 ₂ /0 ₂ /90 ₂ /O ₂
O ₅	TC, FBG	0 ₇ /90 ₈
Metal/O ₂	TC, FBG	O ₈
Metal/O ₂	TC, FBG	90 ₂ /O ₂ /90 ₂ /O ₂

FBGs with standard gratings and Thermocouples Type K (TC) for strain and temperature measurement respectively were placed centrally in the indicated layers. Their positions in the layup were chosen to avoid the neutral axis and determined by a preliminary simulation with Esacomp (Altair). In the hybrid laminate, the cable of the TC was put in the layer adjacent to the FBG, however, the sensor tip was pushed through in the layer to measure in the immediate vicinity of the FBG. The position of the FBG in the layup after processing was confirmed by investigating cross-sectional cuts. For the analysis, FBGs and an interrogator of the company Miopas were used.

3. FBG strain and temperature calibration

In order to carry out quantitative measurements, FBGs have to be calibrated for strain, temperature and pressure. The aim was to identify a sensor signal at corresponding temperatures and strains respectively, to calibrate one influence at a time. As recommended by the manufacturer, the calibration was carried out with the sensor embedded in the host material used in the actual experiments, to account for the shear deformation of the coating, and moisture and bounding conditions of the sensor to the host material [5]. Strain and temperature calibration were carried out using a tensile test machine (Zwick, 20kN) with a climate chamber on a 4mm thick UD CFPA6 specimen ([0₅/FBG/0₁₅]). Data was analyzed using Matlab scripts. No measurable effect on the embedded FBG was evident when applying the maximal pressure on the specimen in the thermoforming press. Therefore, no pressure calibration was carried out.

Based on [4,5], it was assumed that FBGs from the same series have the same sensitivity but could have a different strain-free wavelength λ_0 , at which the FBG is experiencing zero strain. Instead of the measured wavelength (λ) or a normalized wavelength $\frac{\lambda - \lambda_0}{\lambda_0}$, a change of wavelength $\Delta\lambda = (\lambda - \lambda_0)$ was used for the calibration to compensate for potential influences of varying values for λ_0 in different sensors.

3.1 FBG strain calibration

For the strain calibration, strains of 0.14% were applied at 50° and 100°C and held for 5 minutes, exceeding the minimal recommended strain value of 0.1% in VDI/VDE2660. Preliminary tests confirmed a linear relationship between the change in wavelength $\lambda - \lambda_0$ and strain ϵ (eq. 1):

$$\lambda - \lambda_0 = k\epsilon + d \quad (1)$$

where k and d are fitting parameter. To evaluate the measured data, the strain-free wavelength λ_0 was set at 215°C. At this temperature the material solidified sufficiently to ensure slip-free bonding of the sensor while the sensor can still be considered strain-free, i.e., establishing a zero-strain baseline. Parameters k and d were determined by a least square regression. The slope k is divided by λ_0 to make it comparable with normalized measurements, amounts to 0.7875, representing good agreement with the correlation of 0.78 between wavelength and strain found in the literature. [1]

3.2 FBG temperature calibration

The test plate was heated to 20, 50, 100, 150 and 200°C and held for 3 min to realize plateaus in the temperature profile. Temperature was measured with a TC embedded in the plate. During temperature calibration, the specimen was clamped on the upper edge and free to expand otherwise.

There are two temperature related influences on the detected wavelength of the FBG: Firstly, the thermal strain due to expansion of the host material $(\lambda - \lambda_0)_{\alpha(T)}$, which is the desired parameter to be measured during the manufacturing process. Secondly, the change of the refractive index of the FBG i.e., the thermo-optical effect $(\lambda - \lambda_0)_T$, which needs to be both calibrated and compensated for, from the total change in wavelength. The measured shift in wavelength $(\lambda - \lambda_0)_{tot}$ is the sum of those influences.

The thermal strain of the host material can be calculated using the (temperature dependent) coefficient of thermal expansion (CTE(T)) of the host material, which was measured in fiber direction from 30 to 190°C via thermo-mechanical analysis (TMA) and approximated by a polynomial fit. Outside of the measurement interval, the CTE was assumed to be constant. The calculated thermal strain can be converted into a shift in wavelength $(\lambda - \lambda_0)_{\alpha(T)}$ using Eq. (1).

Subtracting the shift of wavelength due to thermal expansion or contraction $(\lambda - \lambda_0)_{\alpha(T)}$ from the total wavelength shift $(\lambda - \lambda_0)_{tot}$ results in the temperature sensitivity or thermo-optical effect of the FBG $[\lambda - \lambda_0]_T$:

$$(\lambda - \lambda_0)_T = (\lambda - \lambda_0)_{tot} - (\lambda - \lambda_0)_{\alpha(T)} \quad (2)$$

A quadratic model was fitted to eliminate the thermo-optical effect:

$$(\lambda - \lambda_0)_T = p_1 * T^2 + p_2 * T + p_3 \quad (3)$$

For temperature measurements, TCs were used instead of FBGs because of the significantly lower costs and reusability. A comparison between temperature measurement of TC and FBG confirms a neglectable difference in measurement accuracy resulting in a neglectable difference in the measured strain (*Figure 1*).

Therefore, the strain is calculated from the measured temperature and wavelength as Eq. (4):

$$\varepsilon(\lambda, T) = \frac{(\lambda - \lambda_0)_{measured} - p_1 * T^2 + p_2 * T + p_3}{k} \quad (4)$$

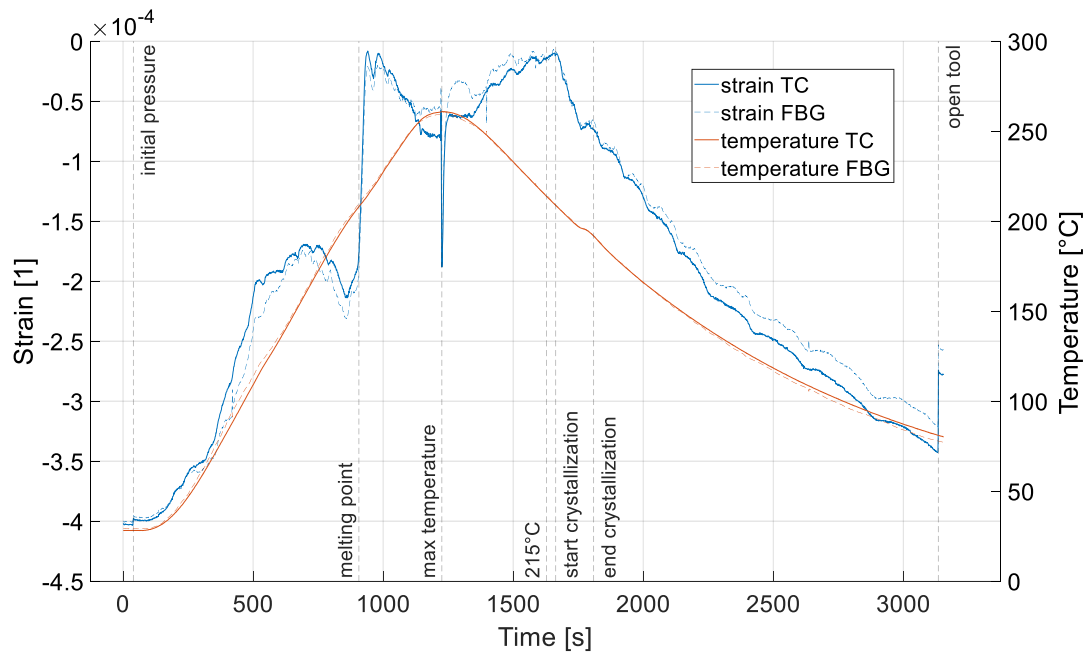


Figure 1. Comparison of strain results based on temperature measurements via TC and FBG

4. Sample manufacturing

The plates were manufactured in a thermoforming press. CFRP plates comprised 20 unbonded 0.2 mm thick prepreg layers. Hybrid plates comprised 10 unbonded prepreg layers and a 2mm thick metal sheet, coated with the adhesion promoter Vestamelt. A small silicon hose at the exit point of the FBG from the laminate prevents breakage of the glass fiber. The layup was heated to 260°, followed by a 2 min hold for temperature homogenization and the application of 100kN pressing force. Maintaining the pressure, the cool down to 80°C is accelerated by active ventilation, followed by demolding and subsequent cooling at ambient temperature.

5. Results and Comparison with process simulation:

The recorded FBG strain and TC temperature are shown in *Figure 2*, and several key events (initial pressure, melting point, max temperature, etc.) in the manufacturing process are indicated. The measured signal contains a superposition of crystallization shrinkage and cooling shrinkage. Crystallization initiates at 200°C and is mainly completed at 185°C, visible as steeper slope in shrinkage strain, followed by a transition to constant shrinkage due to cooling. Based on the exothermic nature of the crystallization process, the temperature curve during crystallization shows a steeper increase in compressive strain. The measurement is stopped shortly after demolding. The next recorded data point is at room temperature, causing the apparent step as the cool down process from demold temperature to room temperature is not depicted.

The effect of temperature on the measured strain in the FBG depends on the current state of the laminate, i.e., in a solid state the CTE of the laminate must be considered, while in the molten state only the CTE of the fiber affects the FBG via friction. Because of these different embedding conditions of the FBG in molten and solid state and material consolidation (unbonded layers prior to heating) the strain results of the measurement can only be evaluated quantitatively

after a reliable connection of the sensor to the laminate is established, i.e., after 215°C at cooling. Experiments with the same layup led to the same qualitative result but an offset in strain, indicating a stable process and measurement system.

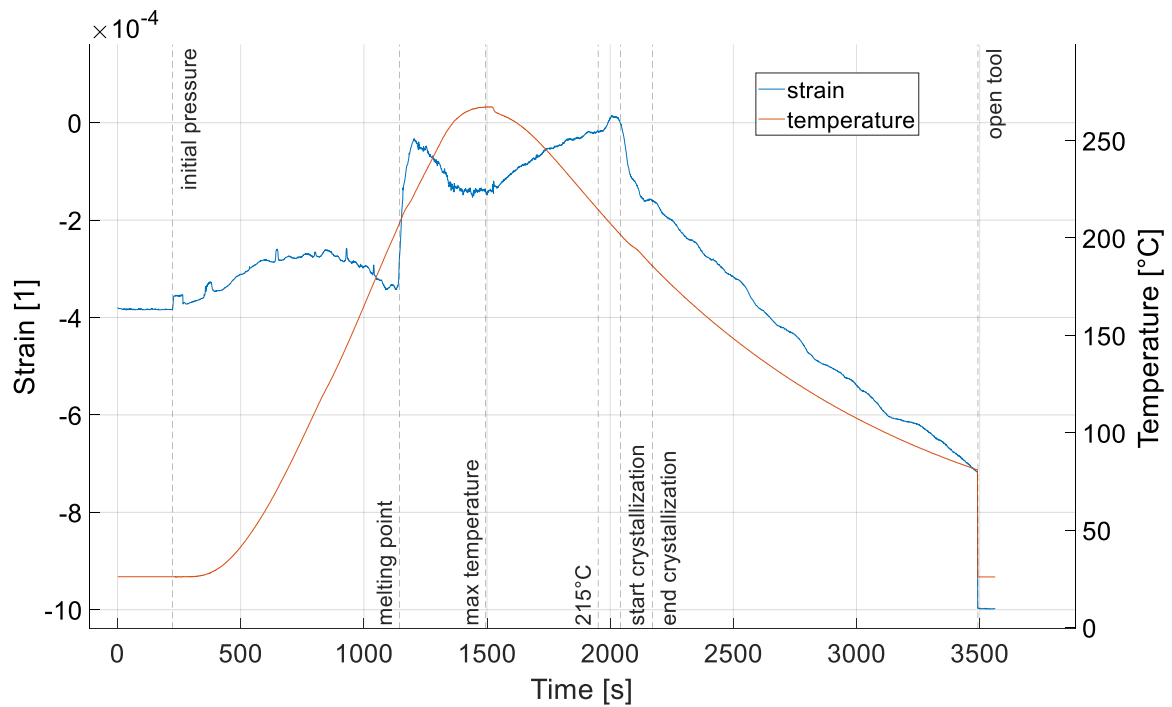


Figure 2. Measured strain (blue) and temperature (orange) from the FBG during the manufacturing of $[Steel/O_2/90_2/O_2/90_2/O_2]$ with key steps being highlighted

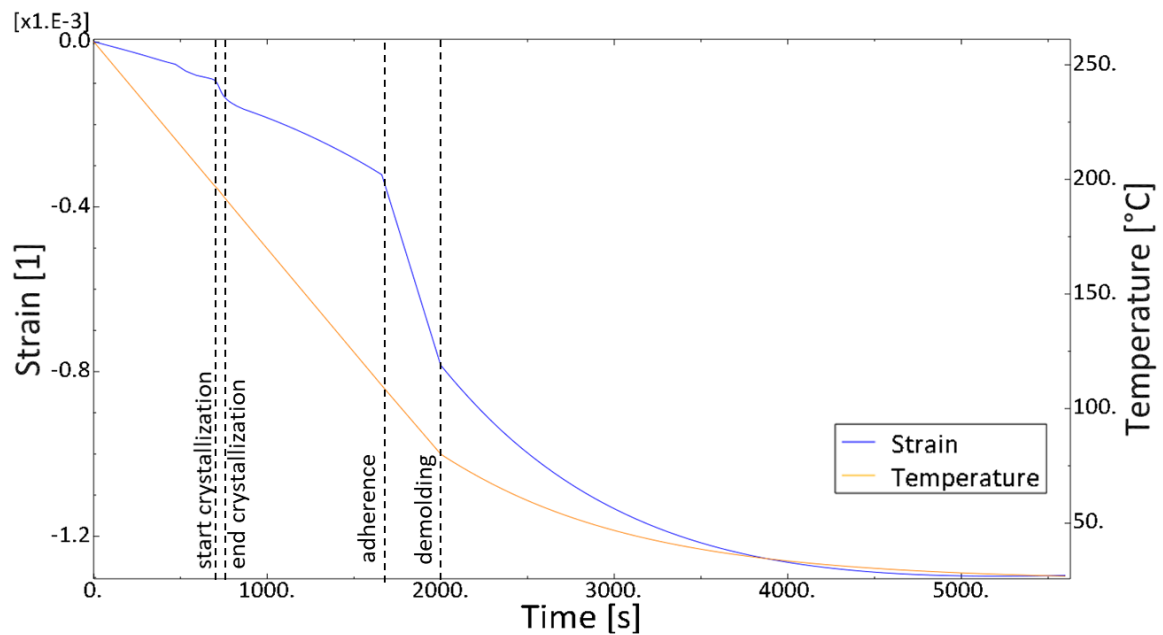


Figure 3. Resulting strain (blue) and temperature (orange) of the cool down and warpage simulation of $[Steel/O_2/90_2/O_2/90_2/O_2]$ layup

Results of the measurements were compared with cool down and warpage simulation results of the respective layer the FBG was put in (*Figure 3, Table 2*). These simulations were implemented in Abaqus using the COMPRO (Convergent) plug-in and model the cool-down behavior from 260°C to 20°C based on a constant cooling rate of 5.5°C/min. Material characterization was performed according to [6]. *Figure 3* depicts the entire simulated cooling process, showing the crystallization at roughly 750s and the demolding at 2000s. The sharp decrease after 1660s stems from reaching 110°C which is the chosen adherence temperature of constituents. This behavior is not shown in the experiment and is attributed to modelling the adherence behavior in the simulation. It is modelled with a discrete step at 110°C but the experiment suggests a continuous transition from sliding to bonding. However, the additional modelling effort was outside the scope of this study. In contrast to the measurement in *Figure 2*, cooling after demolding is included in *Figure 3*. Strain measurement results are in good agreement with the simulated strain.

*Table 2: Measurement and simulation results for residual strains after cool down and demolding (3500s in Figure 2, 5600s in Figure 3). The * indicates that only of valid specimen was tested for this configuration.*

	Material Combination	Measurement Strain [10 ⁻³]	Simulation Strain [10 ⁻³]
CFRP	[O ₂ /90 ₂ /O ₂ /90 ₂ /O ₂]s	-0.56	-0.55
		-0.49	-0.55
	[O ₁₂ /90 ₈]*	-0.59	-0.37
CFRP-metal hybrid	[Al/O ₁₀]	-0.68	-0.95
		-0.67	-0.95
	[Al/O ₂ /90 ₂ /O ₂ /90 ₂ /O ₂]	-1.22	-1.3
		-1.17	-1.3
	[Steel/O ₁₀]	-0.47	-0.85
		-0.47	-0.85
	[Steel/O ₂ /90 ₂ /O ₂ /90 ₂ /O ₂]	-1.00	-1.1
	-1.27	-1.1	

The measurement strains depend strongly on the CTE of CFPA6 in fiber direction. A relatively large deviation in the specimen tested with TMA has been found. Using those individual results from TMA, an increase in strain of $1.5 \cdot 10^{-4}$ compared to the results in *Table 2*, representing a 12% to 30% deviation, can occur. Therefore, a larger sample size with precisely aligned specimen, to account for the dependency on the fiber orientation, must still be realized to improve the data. A potential explanation for variability is assumed to be fiber orientations deviating from 0°, therefore samples will be investigated prior to testing.

The extent of the thermo-optical effect is different for each sensor, therefore an exact result would require the calibration of each sensor. The deviation from the exact result is approximately $2 \cdot 10^{-5}$, so one order of magnitude smaller than the result and therefore neglectable. This effect is also responsible for λ_0 not being at 0 strain in *Figure 2*.

The definition of temperature at which residual strains start to build up, i.e. the stress free temperature can be chosen differently. [7,8] argue that the stress free temperature is found near peak crystallization temperature and before that potential stress build up can be relaxed via molecular chain movement. The difference amounts to about $2 \cdot 10^{-5}$ and was determined to be neglectable.

6. Conclusion

A process monitoring method for residual strain in CFRP and CFRP-metal hybrids was established with FBGs. In order to interpret the measurement data quantitatively, strain and temperature calibrations were carried out on a UD-CFRP plate. In the in-situ strain monitoring during the manufacturing process of CFRP-metal hybrid plates several key events such as crystallization are recorded. Measurement data is in good agreement with simulations of the crystallization kinetics and the residual strains in the manufactured part.

Acknowledgements

We gratefully acknowledge the financial support of the Upper Austrian Government under the FTI-structural-funding program in the scope of the project 'Erforschung von Methoden für die Mobilität der Zukunft', project number "Wi-2018-466449/18-WieM".

7. References:

1. Dobb H, Webb DJ, Kalli K, Argyros A, Large MCJ, van Eijkelenborg MA, et al. Continuous wave ultraviolet light-induced fiber Bragg gratings in few- and single-mode microstructured polymer optical fibers. *Opt Lett* [Internet]. 2003;161(8):417–82.
2. Lee B. Review of the present status of optical fiber sensors. *Opt Fiber Technol.* 2003;9(2):57–79.
3. Friebele EJ, Askins CG, Bosse AB, Kersey AD, Patrick HJ, Pogue WR, et al. Optical fiber sensors for spacecraft applications. *Smart Mater Struct.* 1999;8(6):813–38.
4. Prussak R, Stefaniak D, Hühne C, Sinapius M. Evaluation of residual stress development in FRP-metal hybrids using fiber Bragg grating sensors. *Prod Eng* [Internet]. 2018;12(2):259–67. Available from: <http://dx.doi.org/10.1007/s11740-018-0793-4>
5. Gmbh M. User Manual MIOPAS Interrogator SPK-155. 2020;
6. Gordnian K. Crystallization and Thermo-Viscoelastic Modelling of Polymer Composites. University of British Columbia; 2017.
7. Nairn JA, Zoller P. Matrix solidification and the resulting residual thermal stresses in composites. *J Mater Sci.* 1985;20(1):355–67.
8. Jeronimidis G, Parkyn AT. Residual Stresses in Carbon Fibre-Thermoplastic Matrix Laminates. *J Compos Mater.* 1988;22(5):401–15.

ADVANCED MULTIFIELD MODELS FOR WAVES PROPAGATION ANALYSIS IN METALLIC PANELS

Jamal, Najd^{a,b}, Enrico, Zappino^a, Erasmo, Carrera^a, Walid, Harizi^b, Zoheir, Aboura^b

a: Mul2 Group, Department of Mechanical and Aerospace Engineering, Politecnico di Torino, Torino, Italy (jamal.najd@polito.it)

b: Université de Technologie de Compiègne, Roberval, Compiègne Cedex, France

Abstract: *Active health monitoring of structures throughout their life cycle is a privilege in the different industrial domains. However, it is essential to the domains where the structures are made of composite materials due to the complex damage mechanisms involved compared to metals [1] and due to the absence of an accurate numerical model that permits the prediction of their failure. In this work, the assessment of a multifield layer-wise finite element dynamic plate model (MUL2) based on the Carrera Unified Formulation (CUF) is conducted, on an isotropic aluminum material strip, in order to verify the validity of the model and to finely tune the parameters needed to accurately model wave propagation in the future in laminated material of orthotropic nature. The convergence of the plate model was studied under different modeling parameters, including mesh density, to-the-thickness kinematic model, plate element type and the number of timesteps.*

Keywords: Wave propagation; Lamb waves; Plate model; Carrera Unified Formulation (CUF)

1. Introduction

Composite structures have by nature a complex damage mechanism. This requires the use of different measures to monitor the health of structures made by these materials. The use of various non-destructive testing (NDT) approaches has been studied for the past several decades so that the health of the structure can be determined without affecting its integrity. This is where the application of elastic guided waves propagation in structures excelled for the inspection of structures. Out of these waves, we can mention and focus on Lamb waves that propagate in elastic solid plates with free boundaries. These waves have a displacement direction that is both parallel and perpendicular to the midplane of the plate. Lamb waves have two unique modes of propagation found in isotropic plates, known as symmetric (S) and antisymmetric (A) modes. They are characterized of being the dispersive kind, and the number and nature of modes propagating in a plate depends on the excitation frequency imposed [2]. It can be noticed that for the lower values of frequency-thickness, the excited modes are the fundamental S_0 and A_0 modes exclusively. Among these modes, it is desired to choose the excitation frequency-thickness so that the dispersion effect is relatively low. This can be done by plotting the solution equations of the Lamb wave propagation, named dispersion curves and checking the domain where the velocities are almost constant. As the propagation of these waves is fairly simple in isotropic materials, the taken example under which convergence was studied involves an isotropic aluminum strip. This is also due to the validity of a benchmark with all the properties needed to model wave propagation.

2. Refined Numerical FE Model

The numerical FE model utilized is the MUL2 model, which is based on the Carrera Unified Formulation. In this model, the mechanical 3D displacement vector $u(x, y, z)$ can be split into two terms. The first term, along the xy plane, which has to do with the FEM 2D mesh, and a second term, along the thickness z , that deals with the kinematics of the used model.

$$u(x, y, z) = u_{\tau}(x, y) \cdot F_{\tau}(z)$$

In commercial FEM programs, it is possible to tune the first terms by deliberately reducing mesh size, increasing the mesh density, or by changing the type of the shell element used. However, it is not possible to tune the second item which deals with the plate kinematics. This means that no matter how much the refined mesh may be, the solutions available can not deliver highly accurate results compared to a 3D model. Using a higher order expansion to-the-thickness allows for the modeling of 3D problems using plate models. This higher order expansion can either be in the form of an equivalent single layer (ESL) referred to as TE, where the whole plate thickness is considered as one layer and Taylor Expansion polynomials are used to the specified order; or it can be a Layer-wise expansion (LW) referred to as LE, where Lagrange Polynomials (linear B2, quadratic B3, or cubic B4) are used in each layer.

In TE for the n^{th} order (TE n), the second term $F_{\tau}(z)$ is written in the terms of z^n where n is the order of the expansion. Taking the third order as an example, the general displacement is given as:

$$U = 1.U_0 + z.U_1 + z^2 U_2 + z^3 U_3$$

Where U_i are the unknowns of the problem and U representing the displacement vector $\{u, v, w\}$

For LE on the other hand, and taking the linear B2 element as an example, the displacement vector U can be written in terms of linear Lagrange polynomials F_1 and F_2 as:

$$U = F_1 U_1 + F_2 U_2$$

Where U_1 and U_2 are the actual displacements at the top and the bottom of the plate element, and the polynomials F_1 and F_2 are given by:

$$F_1 = \frac{1 + \zeta}{2} \quad \text{and} \quad F_2 = \frac{1 - \zeta}{2}$$

Where $-1 < \zeta < 1$. On the top, $\zeta = 1$, $F_1 = 1$ and $F_2 = 0$. On the bottom, $\zeta = -1$, $F_1 = 0$ and $F_2 = 1$

It can be referred to [3,4] for more information about the Taylor and in refined plate models.

3. Benchmark problem

In this work, the propagation of both fundamental modes was studied using a dynamic numerical analysis which composes of an assessment of the problem regarding the different numerical parameters. In order to efficiently compare the different variations, it is important to specify a guideline to compute the propagation of the ultrasonic waves. The used setup was the one mentioned in [2]. The wave propagation was studied in a thin plate of a 2 mm thickness, a width of 10mm and a length of 500mm. A set of boundary conditions was applied at the boundaries along the width limiting the displacement in the X-axis and ensuring the

unidirectional propagation of the wave along the y direction. A left boundary condition was applied at the plane $y=0$ as proposed by the benchmark reference mentioned above. The shape of the excitation force imposed is shown in Eq. (1). The two forces are applied perpendicularly and of equal magnitude through time. However, the direction of the forces might differ. Opposite forces produce symmetric waves whereas if both forces have the same direction, antisymmetric waves are generated. In this paper, the applied forces are of opposite direction leading to fundamental symmetric wave generation (S_0). The shape of the load is shown in Eq. (1),

$$F(t) = \tilde{F} \sin \omega t \sin^2 \left(\frac{\omega t}{2n} \right) \quad (1)$$

where $\omega = 2\pi f$ represents the proper pulsation with the central frequency f and n represents the number of cycles within the signal. The central frequency was chosen so that there would be only a single mode of excitation present, such that $f \cdot d < 1.5 \text{ MHzmm}$ according to the dispersion curves in Figure 1 of a 2mm thick aluminum plate of mechanical characteristics found in Table 1.

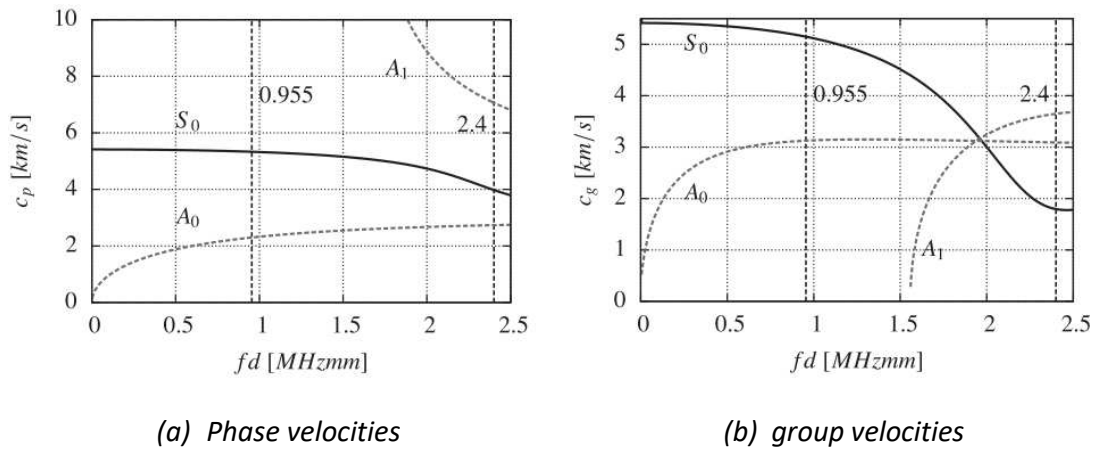


Figure 1. Dispersion curves of 2mm aluminum plate showing (a) phase and (b) group velocities of the antisymmetric modes (A_i) 'dashed' and the symmetric modes (S_i) 'continuous' [2]

For this reason, the excitation frequency was chosen to be $f = 477.5 \text{ kHz}$ with $n = 32$. To study the convergence behavior, two points were chosen (A and B) located on the top of the plate and on the midplane. The position of these points along the y-axis is respectively l_A and l_B (Figure 2)

Table 1 . Material data for aluminium

Youngs modulus (E)	Poisson's ration (ν)	Mass density (ρ)	Longitudinal speed (c_y)	Transversal speed (c_x)
$7 \times 10^{10} \frac{N}{m^2}$	0.33	$2700 \frac{kg}{m^3}$	$6197 \frac{m}{s}$	$3121 \frac{m}{s}$

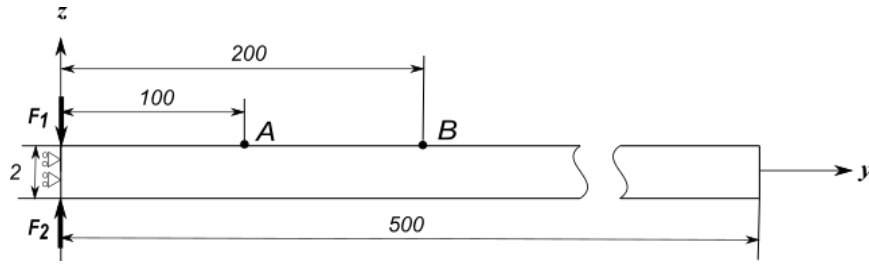


Figure 2. Benchmark of a 2mm aluminum plate showing the distances and the applied forces

4. Evaluation Methodology

The quality of the numerical tool was determined by numerically computing the time-of-flight (TOF) of the propagating Lamb wave packet between points A and B in Figure 3, and comparing this time to an analytical time, computed here by assuming a wave velocity similar to that of the analytical group velocity from the dispersion curves, according to the mode being excited (Table 2). In order to estimate the time at each point, the envelope of the propagating wave had to be generated from the u_z displacement using the Hilbert transform Eq. (2 & 3).

$$H_{A,B}(u(t)) = \frac{1}{\pi} \int_{-\infty}^{\infty} u_{A,B}(\tau) \cdot \frac{1}{t-\tau} d\tau \quad (2)$$

$$e_{A,B} = \sqrt{H_{A,B}(u(t))^2 + u_{A,B}(t)^2} \quad (3)$$

Table 2. Phase and group velocities obtained from dispersion curves [4]

$c_{pS_0} \cong 5316 \frac{m}{s}$	$c_{pA_0} \cong 2298 \frac{m}{s}$
$c_{gS_0} \cong 5130 \frac{m}{s}$	$c_{gA_0} \cong 3126 \frac{m}{s}$

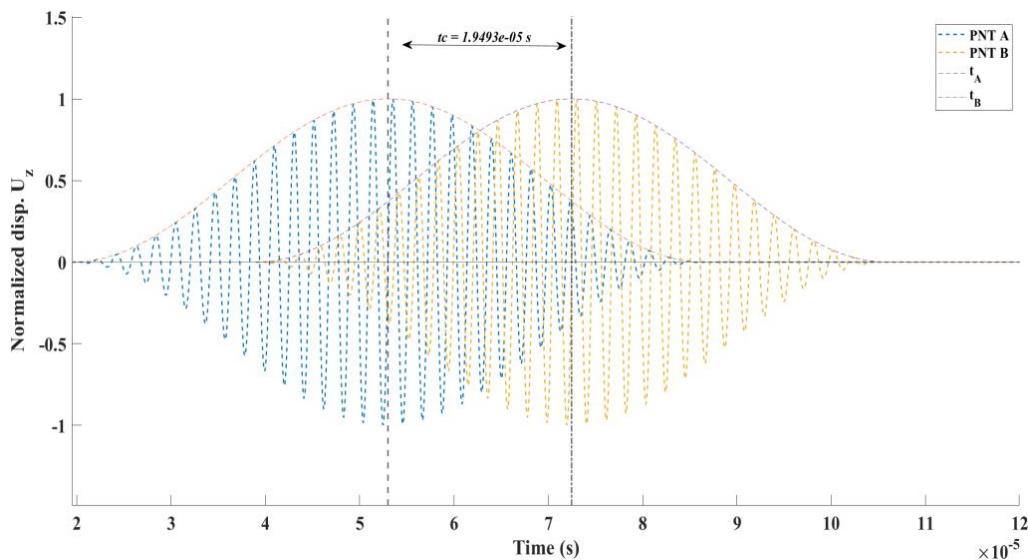


Figure 3. Normalized analytical displacement U_z at points A and B with $t_{c_{ana}}$

The centroid representing the time of each envelope was obtained Eq. (4). This was done using MATLAB commands and coding. The difference of the computed time between point B and A denoted by t_c . Eq. (5) is the time needed for the wave to travel from point A to B.

$$t_{A,B} = \frac{\int_0^{t_{end}} e_{A,B}(t).t dt}{\int_0^{t_{end}} e_{A,B}(t)} \quad (4)$$

$$t_c = t_B - t_A \quad (5)$$

And the calculated relative error is the percentage difference between the analytical and the numerical TOF of points A and B, it is calculated as it is seen in Eq. (6)

$$Error (\%) = \frac{t_{c_{ana}} - t_{c_{num}}}{t_{c_{ana}}} \times 100 \quad (6)$$

5. Assessment Results and Discussion

5.1 Plate element type

The type of the plate elements used was varied between three. The linear element type consisting of 4 nodes, the quadratic type consisting of 9 nodes per element and the cubic type consisting of 16 nodes per element. These elements are denoted by Q4, Q9 and Q16 respectively. Only one element was imposed to the width and the mesh density to the direction of propagation of the wave was altered between 100 to 2000 elements, 4000 for Q4 elements to show convergence. The results in Figure 4 show the convergence of the error with respect to the degrees of freedom according to the number of elements used in each of the three plate element types. Note that this was done for a fixed to-the-thickness Taylor expansion of the third order TE3 and with 2000 timesteps between 0 and 120 μ s. It can be clearly shown that the higher order elements (Q9 and Q16) converge faster, for a lower mesh density, than the lower order. But these elements already have higher DOF for each element. The low mesh density leads to a stiff structure which explains the high error at the beginning of the curves.

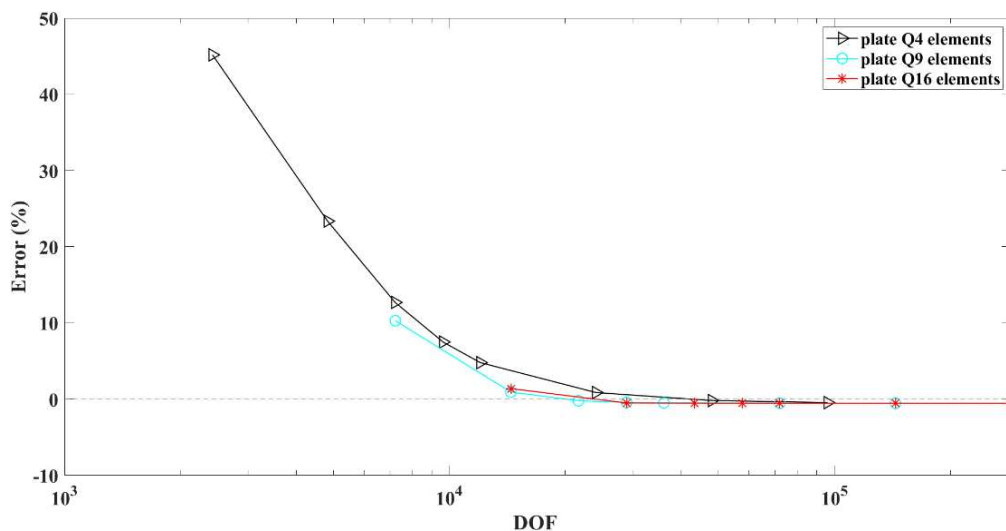


Figure 4. Convergence of different plate element types according to the degrees of freedom

5.2 Model kinematics

The convergence of the problem with different model Kinematics, or to-the-thickness expansion, was also studied in this paper. The Kinematics range between Taylor 1 to 4th expansion, and Lagrange expansion of linear, quadratic and cubic elements denoted by B2, B3 and B4 respectively, where 2B4 means two cubic elements of expansion. These models were compared with one another under the same plate element type, using the same timestep mentioned above (2000 timesteps between 0 and 120 μ s) but under different mesh density to the thickness. The classical plate theories such as classical lamination theory and first order shear deformation theories fail to capture wave propagation through the structure. The results shown in Figure 5 show clearly the convergence of the out of plane expansions to different values. Noting that the linear expansion of both Taylor and the one Lagrange element to-the thickness have exactly the same results with the same DOF. The same goes for TE2 and LE B3, and to TE3 and LE B4. The advantage of using Lagrange expansion lies in the ability to impose boundary conditions on the top and bottom nodes of the plate separately. Also using many elements to the thickness for layered structures, i.e. composites, to accurately depict their behavior.

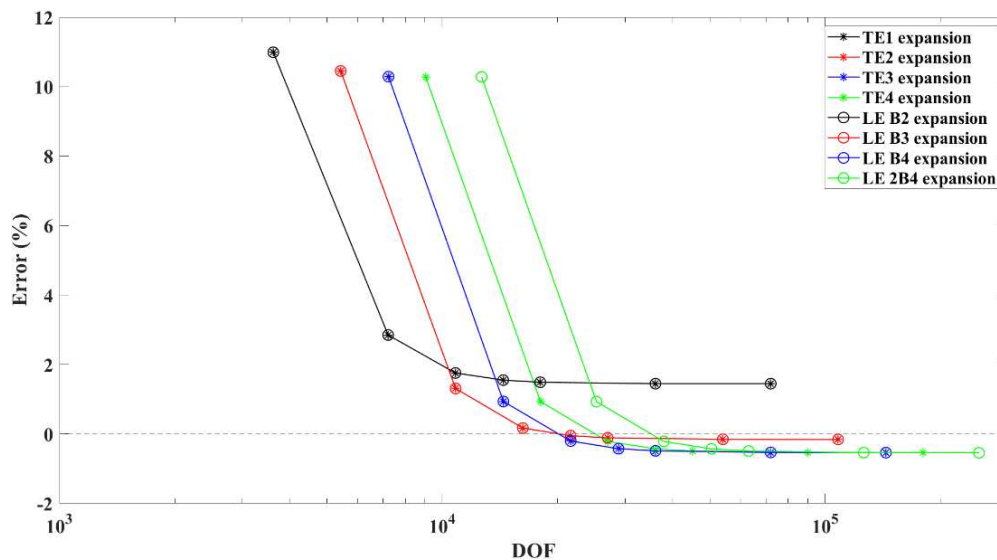


Figure 5. Convergence analysis of the different out of plane expansions according to the degrees of freedom

It is also clearly shown in Figure 6, where the results were plotted with respect to the mesh number along the thickness. It is true that the convergence value of the higher order expansion has a higher error in these results, but this is mainly due to the choice of the timestep as the next results will bring to light.

5.3 Time step analysis

As mentioned above, the effect of the timestep number within the modeling time ranging from 0 to 120 μ s was studied for only one case. The chosen case was a structure having Q9 elements and with TE3 (or LE B4) expansion as these produce the same results for a one layered structure. The reason behind choosing this order of expansion lies in the fact that the higher order expansions used in the comparison (TE4 and LE 2B4) converged to the same values as that of this expansion but for a higher computational cost, see Figure 5. The number of timesteps chosen was 500, 1000, 2000 and 4000. The analysis was done for different mesh densities as earlier.

The results of Figure 7 show the clear relation between minimizing the time step (using more steps) to the convergence towards the analytical value. The lower the timestep is, the more accurate the value of convergence, for the same model kinematics. This is due to the higher accuracy of the imposed variable load at lower timesteps and due to the higher accuracy during the integration of the produced displacement curve under higher value of timesteps.

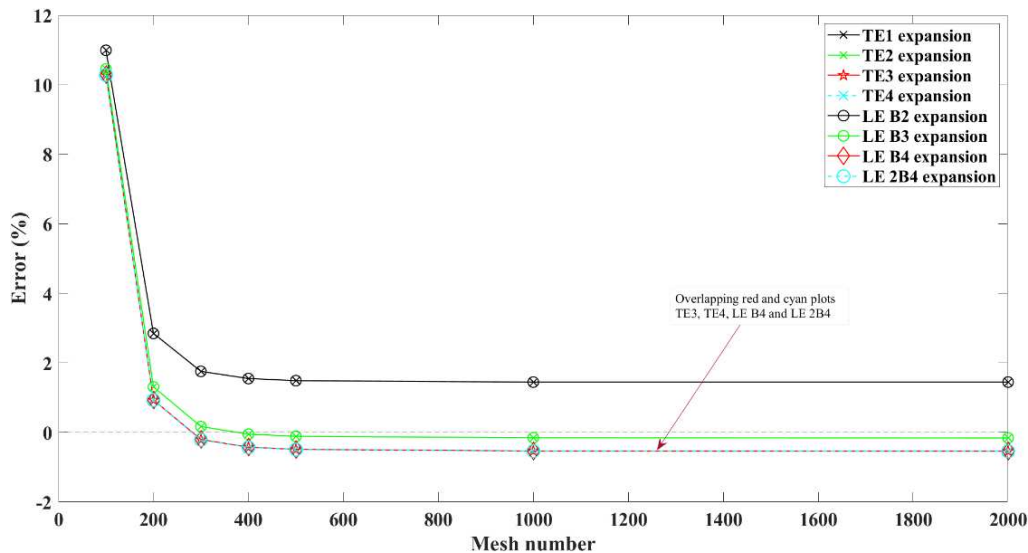


Figure 6. Convergence analysis of the different out of plane expansions w.r.t mesh number

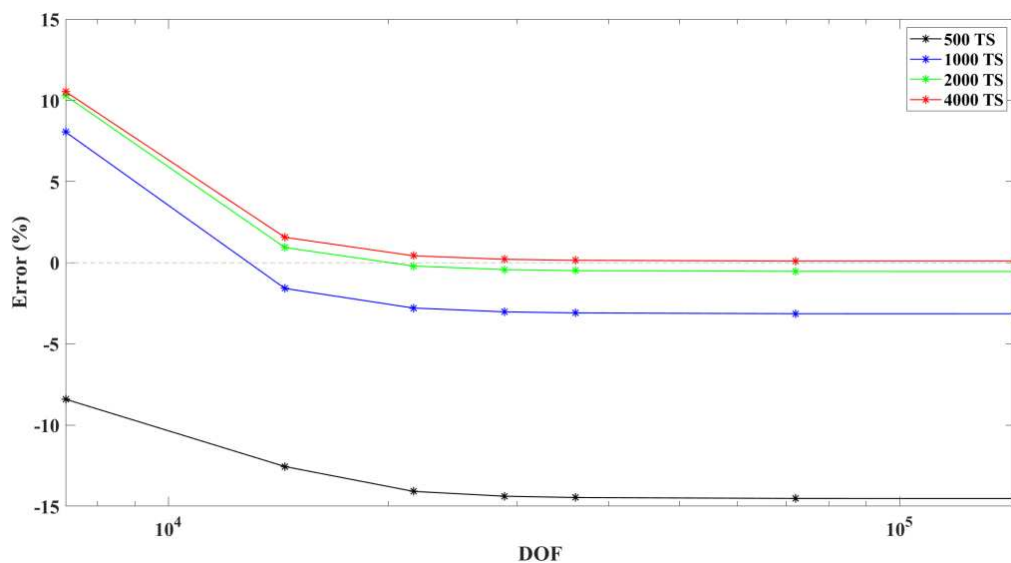


Figure 7. The effect of the number of timesteps (timestep estimate) on the convergence value

6. Conclusion

The numerical assessment of symmetric Lamb wave propagation using a Variable Kinematics model was studied for isotropic aluminum material on the premise of validating the model for further use in laminated and smart structures. The findings of this work show that this model can accurately predict the propagation of the symmetric Lamb waves in isotropic material. If

plate models were to be used, the most suitable element types would be either Q9 or Q16 elements, as Q4 elements are highly not recommended due to the low accuracy. The number of elements used differ according to the element type used, as Q16 elements can reach the same accuracy of Q9 elements for a lower number of elements but on the expense of DOF compared to that of Q9. As for the plate kinematics, or to-the-thickness expansion, the cubic to-the-thickness expansion (TE3 or LE B4) was enough. To reach a higher accuracy in modeling and convergence, a more refined timestep should be used, leading to the use of almost 4000 timesteps in the time domain of the model. To check the validity of the in general expressions mentioned in [4], with a timestep $\Delta t < \frac{1}{20 f_{max}}$ and mesh size $L_{min} < \frac{\lambda}{10}$, and where $\lambda = \frac{c_y}{f}$. In order to get an error of less than 1%, according to our results it is better to choose a timestep $\Delta t < \frac{1}{30 f_{max}}$ with a cubic expansion to-the-thickness, as $\Delta t < \frac{1}{20 f_{max}}$ gives a round 1200 timesteps, leading to a higher convergence error. The minimum mesh size is chosen to be $L_{min} < \frac{\lambda}{8}$ when using Q9 plate elements and $L_{min} < \frac{\lambda}{5}$ when using Q16 plate elements, thus a general mesh size of $L_{min} < \frac{\lambda}{10}$ as proposed in the reference before is acceptable.

Acknowledgements

The authors would like to thank the Hauts-de-France Region (France) and Politecnico di Torino (Italy) for the funding of this work as part of the doctoral thesis of Mr. Jamal NAJD (Agreement number 20003877, N° GALIS: ALRC2.0-000072).

1. References

1. Jollivet T, Peyrac C, Lefebvre F. Damage of composite materials. In: *Procedia Engineering*. Elsevier Ltd; 2013. p. 746–58.
2. Giurgiutiu V. Structural health monitoring with piezoelectric wafer active sensors. 16th International Conference on Adaptive Structures and Technologies. 2006. 94–100 p.
3. Carrera E, Cinefra M, Zappino E, Petrolo M. Two-Dimensional Shell Models with Nth-Order Displacement Field, the TE Class. In: *Finite Element Analysis of Structures Through Unified Formulation [Internet]*. John Wiley & Sons, Ltd; 2014. p. 231–51. Available from: <https://onlinelibrary.wiley.com/doi/abs/10.1002/9781118536643.ch11>
4. Carrera E, Cinefra M, Zappino E, Petrolo M. Two-Dimensional Models with Physical Volume/Surface-Based Geometry and Pure Displacement Variables, the LE Class. In: *Finite Element Analysis of Structures Through Unified Formulation [Internet]*. John Wiley & Sons, Ltd; 2014. p. 253–60. Available from: <https://onlinelibrary.wiley.com/doi/abs/10.1002/9781118536643.ch12>
5. Willberg C, Duczek S, Vivar Perez JM, Schmicker D, Gabbert U. Comparison of different higher order finite element schemes for the simulation of Lamb waves. *Comput Methods Appl Mech Eng [Internet]*. 2012;241–244:246–61. Available from: <http://dx.doi.org/10.1016/j.cma.2012.06.011>
6. GARCIA DE MIGUEL A. Hierarchical component-wise models for enhanced stress analysis and health monitoring of composites structures. Politecnico di Torino; 2019.
7. Alem B, Abedian A, Nasrollahi-Nasab K. Reference-Free Damage Identification in Plate-

Like Structures Using Lamb-Wave Propagation with Embedded Piezoelectric Sensors. J
Aerosp Eng. 2016;29(6):04016062.